Topics in Current Chemistry (2022) 380:37
https://doi.org/10.1007/s41061-022-00387-5

REVIEW

In situ and *Operando* Spectroscopies in Photocatalysis: Powerful Techniques for a Better Understanding of the Performance and the Reaction Mechanism

Houeida Issa Hamoud[1] · Lukasz Wolski[2] · Ilia Pankin[3] · Miguel A. Bañares[4] · Marco Daturi[1] · Mohamad El-Roz[1]

Received: 22 February 2022 / Accepted: 18 May 2022 / Published online: 11 August 2022
© The Author(s), under exclusive licence to Springer Nature Switzerland AG 2022

Abstract

In photocatalysis, a set of elemental steps are involved together at different timescales to govern the overall efficiency of the process. These steps are divided as follow: (1) photon absorption and excitation (in femtoseconds), (2) charge separation (femto- to picoseconds), (3) charge carrier diffusion/transport (nano- to microseconds), and (4 and 5) reactant activation/conversion and mass transfer (micro- to milliseconds). The identification and quantification of these steps, using the appropriate tool/technique, can provide the guidelines to emphasize the most influential key parameter that improve the overall efficiency and to develop the "photocatalyst by design" concept. In this review, the identification/quantification of reactant activation/conversion and mass transfer (steps 4 and 5) is discussed in details using the in situ/*operando* techniques, especially the infrared (IR), Raman, and X-ray absorption spectroscopy (XAS). The use of these techniques in photocatalysis was highlighted by the most recent and conclusive case studies which allow a better characterization of the active site and reveal the reaction pathways in order to establish a structure–performance relationship. In each case study, the reaction conditions and the reactor design for photocatalysis (pressure, temperature, concentration, etc.) were thoroughly discussed. In the last part, some examples in the use of time-resolved techniques (time-resolved FTIR, photoluminescence, and transient absorption) are also presented as an author's guideline to study the elemental steps in photocatalysis at shorter timescale (ps, ns, and μs).

Keywords In situ · *Operando* · Photocatalysis · FTIR · Raman · XAS

This article is part of the Topical Collection "Solar-drivencatalysis"; edited by Nicolas Keller, Fernando Fresno, AgnieszkaRuppert and Patricia Garcia-Munoz.

✉ Mohamad El-Roz
mohamad.elroz@ensicaen.fr

Extended author information available on the last page of the article

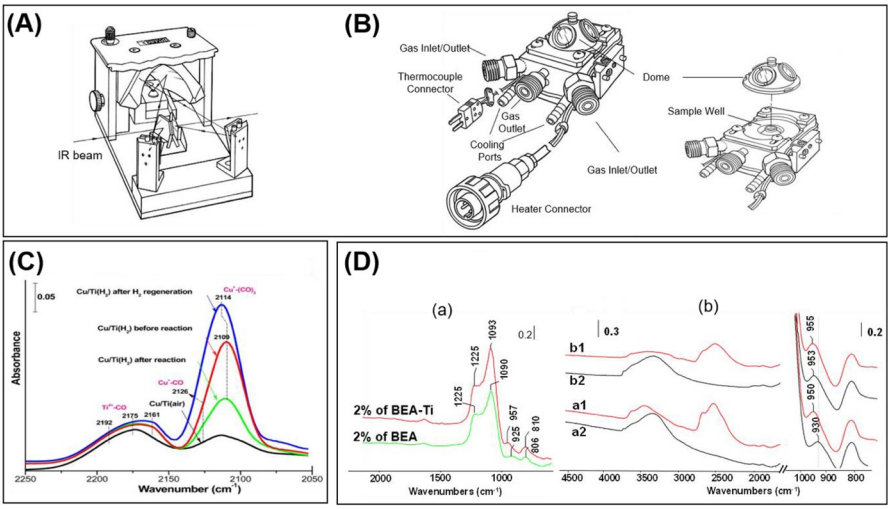

Fig. 1 **A** Interior view of the Praying Mantis diffuse reflectance accessory (DRP) with the model of the high-temperature reaction chamber (HTC), **B** in situ DRIFTS spectra of CO adsorption on Cu/Ti(air) and Cu/Ti(H_2) before and after reaction and after thermal regeneration by H_2, **C** (i) IR spectra of 2% of BEA-Ti (a) and 2% of BEA-ref (b) diluted in KBr and (ii) IR spectra of calcined beta (a) and TiO_2–beta (b) samples diluted in KBr (5 wt%) before (1) and after (2) D_2O exchange. (Copyright with the permission from Refs. [21, 22])

1 Introduction

Photocatalysis is a process in which light energy drives the chemical reactions. This process is initiated by photon absorption and involves at least five separate reaction steps that occur at different timescales, including (1) excitation of electrons upon photon absorption from the valence band (VB) of the photocatalyst to the conduction band (CB), yielding electron and hole pair charge carriers in femtosecond timescale (step 1, Fig. 1), (2) separation (or recombination) of the charge carriers, in femto- to picoseconds [1–3] (steps 1' and 2, Fig. 1), (3) diffusion/transport of the charge carriers from the bulk of the photocatalyst to the surface redox sites, generally in nano- to microseconds [1] (step 3, Fig. 1), (4) activation/conversion of the reactants by their interaction with the charge carriers (oxidation or reduction) in microseconds to milliseconds [4, 5] (step 4, Fig. 1), and finally, (5) mass transfer/diffusion of the reactants and products in milliseconds to seconds [4] (step 5, Fig. 1). Therefore, all these steps, involved together at different timescales, govern the overall efficiency of the photocatalytic process. Thus, each elementary step in photocatalysis must be identified and quantitatively described by performing the appropriate experiments using adequate tools/techniques in order to provide the guidelines for the "photocatalyst by design" concept and improve the overall efficiency. Consequently, it is crucial to describe the different steps which occur from the first interaction of the light with the photocatalyst to the formation of the final products. Thus, it is crucial to identify the electronic structure and the optical properties (bandgap, band positions, absorption coefficient, etc.) of the chosen photocatalyst. These measurements can be achieved

using X-ray absorption and ultraviolet–visible (UV–Vis) absorbance spectroscopy. The femtosecond/picosecond time-resolved absorbance/emission spectroscopies can be also used to investigate the lifetime and the quantum yield of the excited states upon interaction of the photocatalyst with light. After photon absorption and generation of excitons, the latter should be separated to form free charge carriers. This step can be investigated by measuring the exciton binding energy, i.e., the energy required to ionize an exciton from its lowest energy state, using photoemission, optical absorption, photoconductivity screening potential, and magneto-optical spectroscopies [6]. Moreover, density functional theory (DFT) calculations are currently used to estimate the exciton binding energy with high accuracy [7]. The absorption transient and photoluminescence spectroscopies are also useful techniques, in which the quantum yield of the triplet excited state and the quenching rate constants can be determined. Once the exciton is separated, free charge carriers are transferred from the bulk to the surfaces for successful photocatalysis. The conductivity and the redox potential of the photocatalyst in this step can be measured by cyclic voltammetry and conductivity/impedance. Finally, the reaction mechanism/formation of the intermediates can be studied by time-resolved IR spectroscopy from ns–µs (step-scan measurement) to µs–ms (rapid scan measurement); Raman spectroscopy is a molecular spectroscopy that can give complementary information to infrared insight; however, experimental challenges result in the overlap of excitation photons with Raman photons, rendering *operando* Raman spectroscopy more challenging. This review presents approaches to circumvent such hurdle. In situ and *operando* spectroscopies (e.g., infrared (IR), Raman, UV–Vis, X-ray absorption spectroscopy (XAS), among others) may be combined to shed light on the different stages of the photocatalytic act. The diverse techniques used for the characterization and investigation of the various elemental steps in photocatalysis are summarized in Table 1 (Scheme 1).

In this review, we will mainly focus on the in situ and *operando* techniques used in photocatalysis. By definition, in situ spectroscopy, widely used in the catalysis literature, refers to the real-time investigation of catalyst pretreated under vacuum during exposure to the reactants or probe molecules. In situ studies may actually mimic reaction conditions, but the design of in situ cells is typically not that of a catalytic reactor, thus activity data (when measured) are compromised by inappropriate mixing between reactant and catalyst, or temperature gradients, or flow anomalies. Such reaction in situ studies can provide valuable information of the photocatalyst's state in the reaction environment, but cannot deliver reliable activity data. However, "Knowing the before-reaction part or after-reaction part is like studying a life with access only to the prenatal and postmortem states," as mentioned by Gabor Somorjai [8]. That is why birth (catalyst preparation and characterization), life (catalyst in action), and death of catalyst (deactivation) need to be studied [9]. Such consideration has inspired the *operando* methodology, where catalysts are actually working (i.e., *operando*), and their performance is simultaneously determined along with their characterization. *Operando* is a Latin word originally proposed by Prof. M. A. Bañares during a discussion with E. Gaigneaux, G. Mestl, and B. Weckhusen at the 220th ACS National meeting in Washington in 2002 (cf. ref 11 in [8]). Monitoring the catalyst in action, including the observation of reaction intermediates,

Table 1 List of the elemental steps, their properties, and some useful characterization techniques for the photocatalysis process [2]

Elemental step	Properties	characterization techniques
(1) Photon absorption and excitation	-Bandgap -Band positions -Absorption coefficient -Optical penetration depth -Lifetime/quantum yield of singlet excited state	X-ray diffraction UV–visible spectroscopy (for liquids and solids) Femto-/picosecond time-resolved absorbance/emission spectroscopy
(2) Charge separation	-Exciton binding energy -Lifetime/quantum yield of triplet excited state	Optical absorption spectroscopy Photoemission spectroscopy Photoconductivity screening potential spectroscopy Magneto-optical spectroscopy Photoluminescence spectroscopy Transient absorption spectroscopy
(3) Charge carrier diffusion/transport	-Deactivation/quenching of the triplet state -Diffusion length -Conductivity/resistivity -Surface state	Photoluminescence spectroscopy Transient absorption spectroscopy Time-resolved FTIR Conductivity/impedance Cyclic voltammetry
(4 & 5) Reactant activation/conversion and mass transfer	-Activation energy -Rate constant/catalytic activity -Intermediate formation -Molecular structures of the catalyst and reactants -Electronic and geometric structures of transient species	Time-resolved FTIR Transient absorption spectroscopy In situ and *operando* spectroscopies (infrared, Raman, UV–Vis, X-ray absorption spectroscopy [extended AFS (EXAFS) and X-ray absorption near edge structure (XANES)]

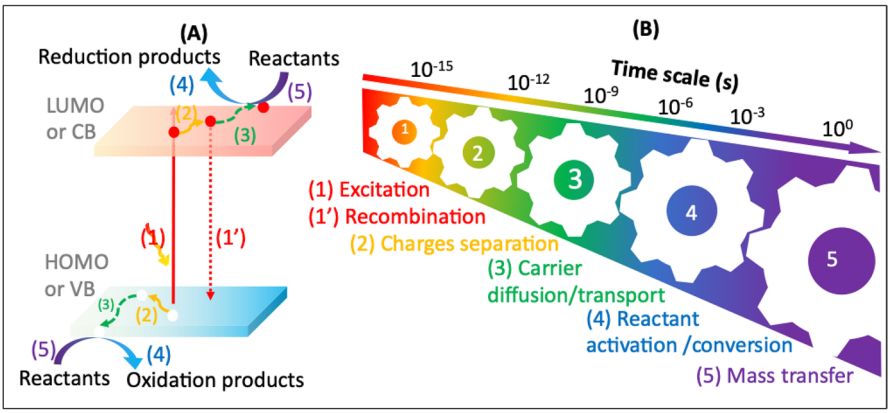

Scheme 1 Illustration of the elemental steps of the photocatalysis process (**a**) occurring at different timescales (**b**)

quantification of metal ions and determination of their oxidation state, and discrimination between spectator species and active sites, is crucial for understanding the reaction mechanism and allows the design of high-performance solid catalysts [10, 11]. For these reasons, many scientific researches have been directed in the last years towards development of *operando* techniques for studying the photocatalytic reaction. Herein, we discuss recent findings related with the most used in situ and *operando* techniques in photocatalysis, such as infrared (IR), Raman and X-ray absorption spectroscopy (XAS). Detailed case studies are presented along with consideration of the methodology and the proper homemade/commercial reaction cells that are designed and adapted to the requirements of the photocatalytic reaction. Special attention is directed toward the identification of active sites and reaction intermediates as well as the investigation of the reaction mechanism (Table 2).

2 In situ Techniques in Photocatalysis

In this section, we will focus on the most popular in situ techniques (FTIR, Raman, EPR, and XAS) used as a characterization tool or to study the reaction mechanism during photocatalysis.

2.1 In situ FTIR Spectroscopy

This technique can operate in three various modes for the present purpose: diffuse reflectance infrared Fourier transform (DRIFTS), transmission, and attenuated total reflection (ATR) (Scheme 2).

Diffuse reflectance originates from multiple reflection, refraction, and diffraction (scattering) at surfaces of small particles within the sample (Scheme 2A) [12]. One of the most important advantages of this technique is the possibility to analyze nontransparent materials at elevated temperatures, which cannot be analyzed

Table 2 List of the advanced techniques reviewed in this article for photocatalysis and their limitations

Techniques	Time resolution	Provided information in photocatalysis	Limitations
FTIR	ms	Identification and quantification of adsorption sites Acidity/basicity and redox properties of photocatalysts: strength and concentration Determination of reaction selectivity and photocatalyst performance/stability or deactivation Discrimination between spectator and active sites Identification of the reaction intermediates under real reaction condition Simultaneous monitoring of photocatalyst's surface and gas or liquid phase to elucidate the reaction mechanism	Very short-lived intermediates cannot be detected Surface-sensitive techniques
Raman	ms	Monitoring changes in surface properties of photocatalysts Identification of the reaction intermediates under real reaction condition	Complementary technique to IR Surface-sensitive techniques Overwhelming of photocatalysis excitation light with Raman photons Low signal intensity resulting from low frequency of the Raman scattering effect Easily affected by fluorescence phenomenon
Electron paramagnetic resonance (EPR)	ms	Tracking electron trapping, recombination, and transfer Identification of radical and reactive oxygen species Direct observation and monitoring of the paramagnetic active species	Performed in the presence of a spin trap and/or at low temperature (below 77 K) in order to improve detection of the highly reactive species with unpaired electrons
XAS (EXAFS and XANES)	ms	Surface- and bulk-sensitive technique Problem of variation in oxidation state, density of unoccupied stats, chemical bond hybridization, bond lengths, and coordination environment	Mainly conducted at synchrotron facilities Limitations in the available experimental setup and the possibility of performing long-term experiments

Table 2 (continued)

Techniques	Time resolution	Provided information in photocatalysis	Limitations
Time-resolved FTIR (rapid and step scan)	ms to ns	Tracking of charge transfer in photocatalysis	Not well developed for *operando* studies in photocatalysis
Time-resolved microwave spectroscopy	ns	Identification of short-lived intermediates	
Photoluminescence	ms to ns	Tracking charge carrier generation, charge carrier trapping, charge carrier recombination, and electron/hole transfer	
Transient absorption	ns to ps	Study the excited-state properties of photocatalysts	
		Lifetimes of photogenerated charge carriers	

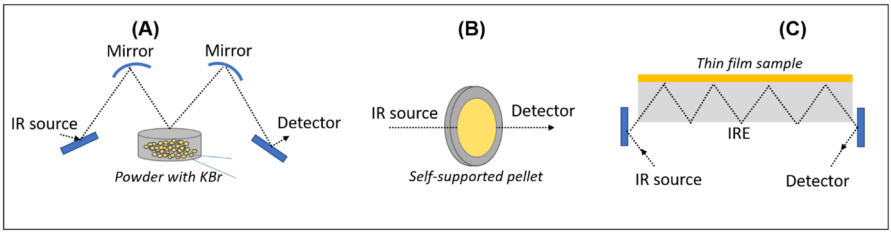

Scheme 2 FTIR spectroscopy in **A** diffuse reflectance, **B** transmission, and **C** attenuated total reflection modes (*IRE* internal reflection element)

by transmission infrared spectroscopy, and easy protocol for the sample preparation. However, this mode presents some limitations for in situ studies such as (1) comparison of samples is challenging due to the different granularity of the sample and (2) quantification of adsorbed species is less straightforward compared to transmission mode. In transmission mode, there are some criteria to be considered, such as (1) particles of catalysts should have size smaller than 2–25 μm in order avoid scattering of the IR radiation, (2) sample pellets (few mg) should be prepared without KBr or any diluent which could react with some gas molecules (e.g., NO to form KNO_3), or it might change the sorption behavior of the sample, and (3) samples should be prepared using a moderate pressure during making pellets to avoid changes in the porous structure of the material and thus of its catalytic performance [13]. However, both transmission and DRIFTS modes are not suitable for liquid analysis, where strong absorption of IR radiation resulting from the presence of the liquid may hinder identification of the signals typical of the solid and of the adsorbates. In the last case, the most appropriate spectroscopic technique is based on the attenuated total reflection (ATR) mode which is suitable for both solid and liquid analysis. ATR-IR spectroscopy exploits an IR-transparent material [internal reflection element (IRE) presenting a refractive index ≥ 2.4, e.g., ZnSe, Ge, Si, diamond] as a waveguide for the total internal reflection at the IRE–medium interface (Scheme 2C) [14]. In ATR-IR configuration, the solid sample is "immobilized" as a thin layer which can be prepared by physical vapor deposition, by drying of a powder suspension, or by chemical growth of the photocatalyst on the IRE, and analyzed via the evanescent wave which penetrates into the sample through ~ 1 μm. In this section, we give some examples of the use of the in situ FTIR technique in photocatalysis.

2.1.1 In situ FTIR Spectroscopy in Photocatalysts Characterization

It is possible to thoroughly characterize the active sites using in situ IR spectroscopy which is highly sensitive to the molecular vibrations and able to distinguish the different geometrical distortions of an adsorbed molecule. In general, two methodologies are used to obtain information on the acidic/redox properties of active sites and on their strength and concentration [15]: (1) the direct observation of active sites and/or (2) indirect characterization using probe molecules. In the first case, the active sites can be directly identified through their IR fingerprints. For example,

the presence of a ν_{OH} band at 3720 cm^{-1} in the FTIR spectrum of TiO_2 confirms the presence of TiOH sites in a defective environment [4]. If the direct investigation of the active site is not possible, the appropriate solution is by the use of an IR probe molecule which can selectively interact with a single active site. However, the choice of a probe molecule must respond to certain criteria such as [16] (1) the molecule size depending on the accessibility of active sites; (2) the spectral response with a significant intensity and spectral sensitivity to the band position depending on the type of interaction; (3) the sufficient interaction with the site under study to obtain valuable information; (4) the stability on the surface catalyst to avoid decomposition; and (5) sufficient vapor pressure to be easily introduced into the IR cell.

The redox properties of photocatalysts can be investigated using CO, NO, and/or methanol as probe molecules [17, 18]. This gives information about the oxidation/coordination state of the active sites, their acidity, and location on the surface. On the other hand, both Lewis and Brønsted acidity of the photocatalyst can be determined using probe molecules with strong basicity such as pyridine, ammonia, lutidine, and trimethylamine. More detailed insight into the nature of the active site can be provided by co-adsorption of probe molecules, while the structure of the adsorption sites can be determined on the basis of isotopic exchange. As far as potential application of in situ IR studies in concerned, it is important to underline that results obtained from adsorption tests at different temperature may be used to determine entropy and enthalpy of adsorption process. Finally, in situ IR experiments may also provide information about the nature of interaction between the reactant and the active site, similar to that observed during the photocatalytic reaction [19, 20]. For example, Liu et al. [21] used DRIFTS in situ adsorption of CO to identify changes in redox properties of the coper species in Cu/TiO_2 catalyst after its pretreatment at 200 °C under hydrogen or air before and after its application in photocatalytic reduction of CO_2 under visible light. The experiments were performed in a Praying Mantis diffuse reflectance accessory equipped with a high-temperature reaction chamber (Fig. 1A) (Harrick Scientific, HVC-DRP). The dome of the DRIFTS cell had two KBr and one quartz windows transmissive to infrared and visible light, respectively (Fig. 1A). The authors found that the Cu/TiO_2 catalyst pretreated under hydrogen ($Cu/Ti(H_2)$) exhibits higher concentration of Cu^+ species compared to Cu/Ti(air), as confirmed by in situ CO adsorption experiments (more intense band at 2109 cm^{-1}, Fig. 1B). This explains the superior photocatalytic activity of $Cu/Ti(H_2)$. The latter was deactivated during the reaction and was not restored even after re-treatment under H_2 at 200 °C, which is related to the higher amount of Cu^{2+} in $Cu/Ti(H_2)$ after reaction and the changes in chemicals surrounding Cu^+ species after the regeneration process. This was evidenced by the shift of the Cu^+-$(CO)_2$ IR band from 2109 to 2114 cm^{-1} (Fig. 1B). In another example, the in situ D_2O exchange was used to verify the possibility of incorporating titanium (IV) oxide in a beta zeolite structure by formation Si–O–Ti bonds during preparation of new photocatalyst by cold $TiCl_4$ plasma process [22]. The IR results show the presence of an important feature at 955 cm^{-1} in the TiO_2-beta sample. The assignment of this band was still in debate; it could be assigned to Si–O–Ti or ν(Si–OH) vibrations. In order to unravel the origin of this IR band, the authors performed isotopic exchange of silanol with 10 mbar of D_2O. After D_2O exchange, the band at 930 cm^{-1} shifted by 20 cm^{-1} in the pure

zeolite sample (Fig. 1C) which is attributed to the H–D exchange of silanol groups. In contrast, a negligible shift (from 953 to 955 cm^{-1}) was observed for the Ti-doped zeolite (Fig. 1C) which undoubtedly confirms the formation of the Si–O–Ti bond. A similar study comparing silica-supported titania with titanium–silicalite and the effect of exposure to hydration also identified the Si–O–Ti bond vibration in the 960–970-cm^{-1} window of titania-silicalite [23].

2.1.2 In situ IR Studies for Investigating Photocatalysis in a Gas Phase

Modified in situ IR cells were also used to study the reaction mechanism over TiO_2 during photocatalytic reaction involving a gas phase. However, this is an indirect method of investigation, since the reaction is performed under special conditions (partial vacuum), and the surface and gas phase analyses are performed separately. Some case studies describing various photocatalytic reactions are presented here. Fu et al. [24] used an in situ DRIFTS cell [Praying Mantis diffuse reflection accessory with a high-temperature reaction chamber (Harrick Scientific)] to compare the reactivity of adsorbed methanol species on {001} and {101} planes of titanium dioxide nanocrystals. The fresh catalyst was loaded into the reaction chamber then evacuated at 40 °C until equilibrium and exposed to methanol or water through glass bulbs until saturation. The photocatalytic reaction was initiated by irradiation with a 100-W high-pressure Hg arc lamp (Oriel 6281). On the basis of in situ DRIFTS data, the authors established that both molecularly and dissociative adsorbed methanol species are photo-active on TiO_2-{101} surface, while in the case of TiO_2 {001}, only methoxy species can be oxidized during the photocatalytic reaction with higher reactivity than those adsorbed on TiO_2-{101} facets. The authors observed that the intensity of an IR band typical of methoxy species adsorbed on TiO_2-{001} (band at ca. 2820 cm^{-1}) was continuously decreasing upon exposure of the catalyst to light, while that of molecularly adsorbed methanol on TiO_2-{001} (band at ca. 2950 cm^{-1}) remained unchanged (Fig. 2A). In the case of TiO_2-{101}, the intensity of IR bands typical of both molecularly (2950 cm^{-1}) and dissociatively (2820 cm^{-1}) adsorbed methanol molecules were decreasing over the reaction time (Fig. 2A).

Another example of the use of in situ DRIFTS was reported by Zhang et al. [25]. The authors investigated the impact of pretreatment conditions on the catalytic performance of TiO_2 in the photoreduction of CO_2. The photocatalysts (60 mg) were pressed into a thin wafer and loaded into the reaction cell. The photocatalytic reaction was then initiated by irradiation with UV light [5-W light emitting diode (LED) lamp; $\lambda = 365$ nm]. The authors found that pretreatment conditions (Ar vs. H_2 for 12 h) have significant impact both on activity and selectivity of TiO_2 catalysts. The main product of photoreduction of CO_2 over Ar-treated catalyst (Ar-12) was the carbon monoxide, while in the case of H_2-treated sample (H-12), the main product was formic acid. It was found that in the case of the Ar-treated sample, CO_2 molecules were bound to the catalyst surface via a bridging bidentate configuration (Fig. 2B; IR band at 1671 cm^{-1}). In this adsorption mode, the carbon dioxide was interacting with two Ti^{3+} sites formed near the oxygen vacancy. In the case of the surface IR spectra of H_2-treated samples (i.e., H-2 and H-12), the authors observed an additional vibrational band at 1576 cm^{-1}, assigned to CO_2 molecules bound to

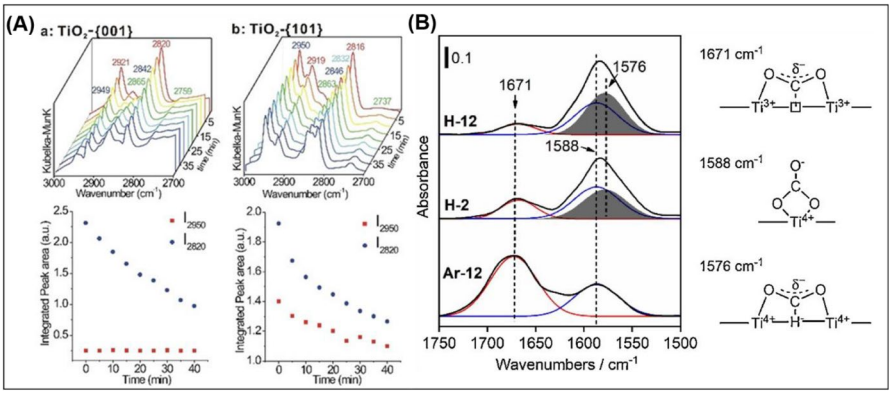

Fig. 2 **A** In situ DRIFTS spectra of TiO_2 during the photocatalytic oxidation of adsorbed methoxy species ($CH_3O_{(a)}$) and molecularly adsorbed methanol molecules ($CH_3OH_{(a)}$) at 40 °C in a 10% O_2/Ar atmosphere with a flow rate of 30 cm^3/min and (bottom) coverages of $CH_3O_{(a)}$ and $CH_3OH_{(a)}$, respectively, represented by the integrated intensity of the vibrational features at 2820 and 2950 cm^{-1}, as a function of photocatalytic oxidation time: a TiO_2-{001} and b TiO_2-{101} nanocrystals (NCs). DRIFTS spectra of corresponding bare TiO_2 NCs were used as the background spectra; **B** FTIR spectra of CO_2 adsorption on the samples of Ar-12, H-2, and H-12 in the region of 1750–1500 cm^{-1}. The background was collected just before the introduction of CO_2. (Copyright with permission from Refs. [24, 25])

hydride-like –Ti–H–Ti– sites via a bridging bidentate configuration (Fig. 2B). This unique CO_2 adsorption mode, observed only for H_2-treated samples, was found to be crucial for formation of C−H bonds and the selective production of formic acid during the photocatalytic reaction. The authors revealed also that the adsorbate characterized by the IR band at 1588 cm^{-1}, observed on both samples pretreated with Ar and H_2, is rather a spectator than an active intermediate species.

The recent in situ IR studies by Subbotina and Barsukov [26] allowed identification of surface peroxides as important reaction intermediates during photocatalytic oxidation of gaseous ethanol over TiO_2. In all the experiments, the authors used a homemade in situ cell in which the photocatalysts were deposited on thin (~0.4 mm) O-shaped Si slabs (8.5-cm diameter). The irradiation was performed with a UV light emitting diode ($\lambda = 365$ nm; 10 mW cm^{-2}). The authors established that exposure of TiO_2 to UV light in moist air led to the formation of surface peroxide species which were identified on the basis of the IR bands at ca. 852, 912, and 973 cm^{-1}. These species are stable in the dark. However, upon UV irradiation, the intensity of the typical IR bands of both ethanol and the surface peroxide species was continuously decreasing over the reaction time. In parallel, several new IR bands characteristic of partial oxidation products (bands at ca. 1130, 1020, 963 cm^{-1}) were observed. Interestingly, when ethanol and other organic intermediates were oxidized, the surface peroxide species were formed again and accumulated on the TiO_2 surface.

Hirakawa et al. [27] reported that the selectivity of photocatalytic reduction of NO_3^- is strongly affected by the surface properties of commercial TiO_2 (JRC-TIO-6). The experiments were carried out using an FT/IR-610 system (Jasco Corp.) equipped with an in situ diffuse reflectance cell (Heat Chamber cold + HC-500, ST Japan, Inc.). Before the experiments, 50 mg of the catalyst was treated with 1.0 M

HNO_3 under continuous stirring for 6 h. The catalyst was then separated by centrifugation and dried at 333 K for 6 h. The catalyst containing NO_3^- species adsorbed on its surface was then placed inside the in situ cell and evacuated at 303 K for 3 h. The photocatalytic reaction was initiated by irradiation with a Xe lamp (300 W; $\lambda > 350$ nm) at 303 K. The results show that the formation of ammonia, as the most desirable product, was observed only in the presence of TiO_2 catalysts with a high concentration of surface defects and a low number of Lewis acid sites, as revealed by in situ DRIFTS analysis. As shown in Fig. 3Aa, exposure of the highly deficient JRC-TIO-6 (8) catalyst to visible light resulted in a significant decrease in the intensity of the IR bands typical of bidentate NO_3^- species adsorbed on TiO_2 defects (IR band at 1610 cm^{-1}), parallel to an increase in the IR band intensity assigned to the ν(H–N–H) deformation in NH_4^+ molecules (band at 1445 cm^{-1}). The latter indicated that NH_3 was successfully formed by photocatalytic reduction of NO_3^-. In the case of the catalyst with a low concentration of defect sites and a high number of Lewis acid sites [JRC-TIO-1 (1)], a significant conversion of NO_3^- was also noticeable, but it was not associated with the increase in intensity of the IR band typical of NH_4^+ (Fig. 3Ac), suggesting that Lewis acid sites promoted the formation of other products of nitrate reduction. Different selectivity of the abovementioned catalysts was explained by different strength of NO_3^- adsorption at the Lewis acid sites (Ti^{4+} ions) and the defect sites (Ti^{3+} atoms adjacent to oxygen vacancies). As depicted in Fig. 3A, NO_3^- species adsorbed on the surface defects were characterized by lower

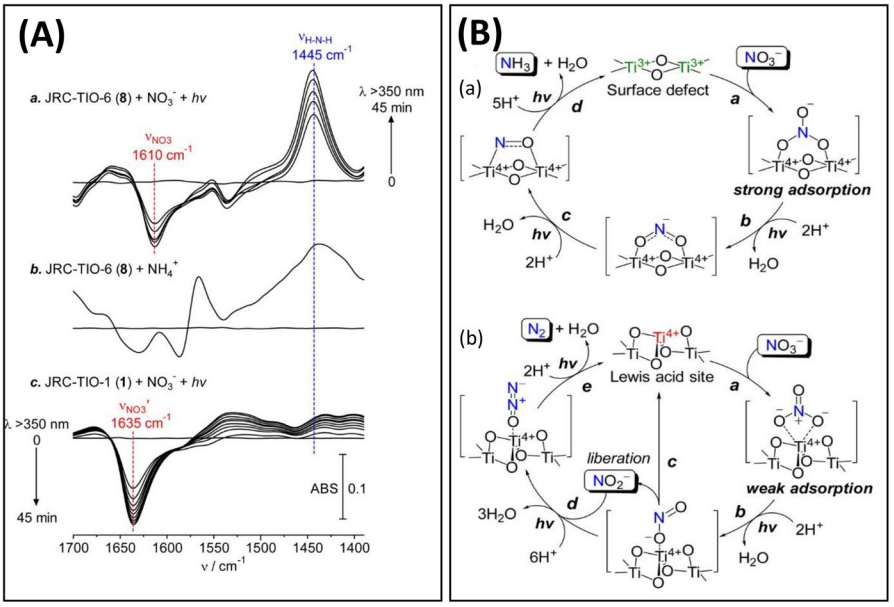

Fig. 3 **A** Time-dependent change in the DRIFTS spectra of NO_3^- adsorbed on (a) JRC-TIO-6 (8) and (c) JRC-TIO-1 TiO_2 (1). The sample after adsorption of NO_3^- was measured at 303 K under photoirradiation ($\lambda > 350$ nm). (b) S spectrum of NH_4^+ (21 μmol) adsorbed on JRC-TIO-6 (8). **B** Proposed mechanisms for photocatalytic reduction of NO_3^- on (a) surface defect and (b) Lewis acid site of TiO_2. (Copyright with permission from Ref. [27])

wavenumbers than those adsorbed at Lewis acid sites (1610 vs. 1635 cm^{-1}, respectively). This shift is attributed to a strong electron donation from the surface defects to the N=O antibonding orbital of NO_3^- species, which enabled much stronger adsorption of nitrates and other intermediate products on the defect-rich sample, and this, in turn, promoted formation of NH_3 instead of N_2 (Fig. 3B).

2.1.3 In situ IR for Investigating Photocatalysis in a Liquid Phase

To the best of our knowledge, the first in situ FTIR photocatalytic study in a liquid phase was related to evaluation of the photocatalytic activity of P25 TiO_2 in mineralization of malonic acid [28]. The authors used ATR-IR spectroscopy combined with modulation excitation spectroscopy and isotope labeling to enhance the sensitivity of the product detection. For this purpose, a dedicated flow-through cell was realized and mounted on an attachment for ATR measurements (Wilks Scientific) within the sample compartment of a Bruker Equinox-55 FTIR spectrometer equipped with a narrow-band MTC detector (Fig. 4A). Thanks to this tool and to the used approach, important mechanistic aspects were revealed. In particular, it appeared that at least two different pathways (concerning contribution of different oxygen sources, namely dissolved oxygen and oxygen from water) lead from the adsorbed malonates to the oxalate after the first photo-Kolbe reaction. Furthermore, dissolved oxygen would influence the rates of the different reaction steps, playing the role of an acceptor of photo-excited electrons, and accelerating the photocatalytic reactions by increasing the efficiency of photo-excited charge carrier separation.

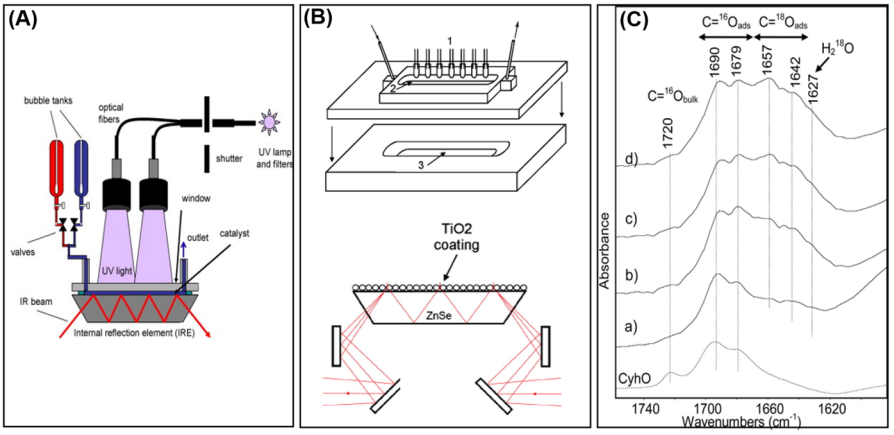

Fig. 4 **A** Schematic setup for in situ ATR-IR spectroscopy of photocatalytic reactions in a small volume flow-through cell. **B** Scheme of the ATR-FTIR cell, including the light source (1), the quartz window on the top plate (2), and the internal reflection element (3) and representation of the IR path and penetration into the TiO_2 coating. In practice, 11 bounces were allowed by the crystal dimensions rather than the three bounces shown; **B** infrared spectra after 10 min of cyclohexane photo-oxidation with 5% $^{18}O_2$/He on a TiO_2 catalyst which has been subjected to oxygen isotopic exchange (OIE) for (a) 0 min, (b) 15 min, (c) 30 min, and (d) 60 min. The black dashed spectrum corresponds to the cyclohexanone (CyhO) adsorption. (Copyright with the authors permission [29, 30])

Another very interesting study reported cyclohexanone photo-oxidation over a TiO_2 film using in situ ATR-FTIR spectroscopy [29]. All photocatalytic reactions were performed with the use of an ATR cell made of quartz with an inner volume of 4 mL (Fig. 4B). The photocatalytic reaction was initiated upon exposure to a 75-W xenon lamp. In order to eliminate radiation below 275 nm, the cell was covered by a Pyrex glass. For in situ ATR studies, water solution of TiO_2 nanoparticles was loaded on the ZnSe crystal of the ATR accessory and then evaporated under vacuum to form a TiO_2 film (Fig. 4B). Before the measurements, the TiO_2 powder was dried at 120 °C for 1 h and pre-illuminated under $^{16}O_2$/He or $^{18}O_2$/He atmosphere. In order to investigate the mechanism of photocatalytic oxidation of cyclohexane, the authors used oxygen isotopic exchange (OIE) to prepare variable amounts of Ti−^{18}OH species on the surface of TiO_2. They found that the dissolved oxygen is not directly involved in the photocatalytic oxidation of cyclohexane and that the main sources of the oxygen in the product of oxidation reaction are TiO_2-associated active sites. Based on the IR results, the cyclohexanone with a C=^{18}O carbonyl group (IR bands at 1657 and 1642 cm^{-1}) was formed only when oxygen isotopic exchange was performed before the photocatalytic process (Fig. 4C).

Belhadj et al. [31] used in situ ATR-IR spectroscopy to investigate the influence of UV irradiation on H_2O adsorption on the TiO_2 surface. The in situ ATR experiments were performed with the use of a FTIR spectrometer (IFS 66 BRUKER) equipped with an internal reflection element of 45° ZnSe crystal and a deuterated triglycine sulfate (DTGS) detector. The TiO_2 film was deposited on the surface of the ZnSe crystal by a simple evaporation method. Firstly, the aqueous suspension of TiO_2 (5.75 g/L) was sonicated for 15 min and placed on the surface of the crystal. Next, water was slowly evaporated at room temperature (RT). The exposure of the TiO_2 film to UV light was obtained with the use of an LED lamp ($\lambda = 365$ nm). Similarly to Subbotina and Barsukov [26], they found that surface hydroperoxy species (Ti–OOH), characterized by a vibrational band at 3483 cm^{-1}, can be formed on TiO_2 only in the presence of molecular oxygen and UV light. The authors also found that exposure of TiO_2 to UV radiation in the presence of oxygen results in the formation of a greater number of surface hydroxyl groups, which in turn enhances the hydrophilicity of the metal oxide.

A new in situ homemade glass reactor equipped with CaF_2 windows has been developed by El-roz et al. (Fig. 5A) for monitoring homogeneous and heterogeneous photocatalytic reactions in liquid phase [32]. The new in situ FTIR reactor is dedicated for a real-time analysis of the gas products in transmission mode, but it cannot provide information on the evolution of the catalyst surface during the reaction. However, it can offer important information on the reaction selectivity and photocatalyst performance. Thanks to the different accessories, the system can operate as a batch or a continuous-flow reactor. The total internal volume of the reactor is 160 mL and can be filled with 10 to 50 mL of solution. The UV–visible irradiation is provided by a Xe–Hg lamp connected to a UV light guide mounted at the top of the IR cell with the possible control of temperature from 25 to 80 °C thanks to an unfixed resistance and a thermocouple. This reactor solves the problems of (1) irradiation homogeneity, (2) solvent condensation, (3) deformation of the O ring in the presence of an organic solvent, and (4) the reactor seal's ability to control leaks,

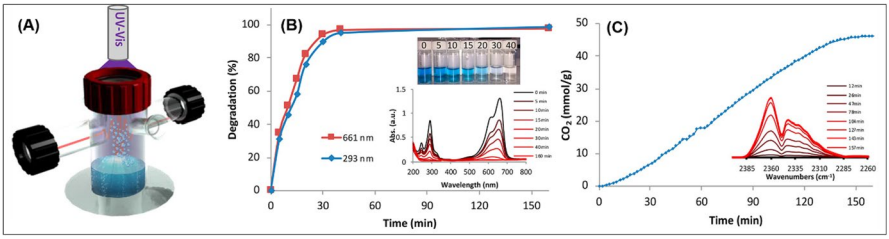

Fig. 5 **A** The new in situ FTIR reactor used for monitoring the gas headspace of a photocatalytic reaction in the liquid phase and **B** evolution of the photocatalytic degradation of MB on TiO_2-P25 versus the irradiation time as determined using UV–visible absorbance of the MB. Inset: the corresponding samples and their UV–visible absorbance spectra. **C** Evolution of CO_2 in the gas headspace. Inset: the FTIR spectra of the headspace in the vibration region of CO_2 at different irradiation times. Reaction conditions: $m_{TiO2} = 50$ mg; $V_{water} = 50$ mL; [MB] = 0.2 mM; lamp, Xg–Xe (200 W); $\lambda = 365$ nm; irradiance, 15 mW/cm^2. (Copyright with the authors permission [32])

which is very important for air-sensitive reaction. The in situ reactor was used to study different kinds of photocatalytic reactions in liquid phase such as formic acid decomposition [32], the photocatalytic CO_2 reduction [33, 34], and the photodegradation of methylene blue (MB) [32]. The latter was performed on TiO_2 P25 under monochromatic irradiation at 365 nm. Using the new reactor, the authors demonstrated that the total discoloration of MB observed after only 40 min of reaction, as shown by UV–Vis measurements (Fig. 5B), is not linked with the total degradation/oxidation of the compound. The evolution of the IR spectra of the reaction head space demonstrates an increase in the CO_2 until reaching a plateau only after 125 min (Fig. 5C), which means 60 min after the total discoloration. Thus, the new reactor allows distinguishing between the discoloration and the total oxidation of the MB, which is widely used as a model to study the photocatalytic degradation performance of dyes.

2.2 In situ Raman Spectroscopy

Raman spectroscopy is an experimental technique that allows identification of chemical compounds by utilizing the Raman effect, in which incident light is inelastically scattered from a sample and shifted in frequency by the energy of the excited molecular vibrations [35]. Depending on the energy of the excitation laser and nature of the material, the incident light may penetrate the samples at a depth ranging from millimeters to nanometers [35]. Thus, this experimental technique may be used not only for the evolution of bulk and surface properties of the photocatalysts (e.g., precise analysis of structure and changes in composition of materials during reactions [36]), but also for tracking transformation of reagents on the catalysts' surface ([37]). In terms of application of Raman spectroscopy in heterogeneous catalysis, one of the most important limitations of this technique is its low signal intensity resulting from low frequency of the Raman scattering effect [38]. This drawback has been overcome by utilizing resonance effects in Raman spectroscopy which resulted in development of new experimental techniques, such as surface-enhanced

Raman spectroscopy (SERS), shell-isolated nanoparticle-enhanced Raman spectroscopy (SHINERS), or tip-enhanced Raman spectroscopy (TERS); however, the applicability of those approaches imposes limitations on characterization of systems and reactions, particularly if *operando* conditions are sought. Recent advances in application of resonance Raman spectroscopy for characterization of nanomaterials and monitoring of catalytic reactions are described in references [35, 39]. As concerns photocatalytic processes, a majority of literature reports in this field are related to application of in situ SERS technique because of its high local sensitivity and spatial resolution that enable precise analysis of surface-adsorbed species. To date, in situ SERS studies have been used mainly for monitoring of numerous plasmon-driven surface reactions, e.g., demethylation of methylene blue [40], degradation of Rhodamine 6 G [41], dehalogenation of 4-iodothiophenol [42], transformation of benzylamine to N-benzylidenebenzylamine [37], and hydrogenation of CO_2 [43], reduction of 4-nitrothiophenol [44], as well as dimerization of para-nitrothiophenol to p,p′-dimercaptoazobenzene [45]. The in situ SERS studies included not only identification of reaction intermediates and products (e.g., [42, 46]), but also detailed analysis of changes in surface properties of catalysts [43].

2.2.1 In situ Raman Spectroscopy in the Photocatalysts Characterization

Recently, in situ SERS studies were applied to investigate the efficiency of hot electron transmission through various materials [47]. For this purpose, gold nanoparticles (Au NPs) were covered with a thin shell of SiO_2, TiO_2, or Pd as a model insulator, semiconductor, and metal, respectively. The as-prepared catalysts were then deposited on Au(111) single crystal covered with a monolayer of para-aminothiophenol (pATP) (Fig. 6A–C). The efficiency of hot electron transfer from Au NPs via shells composed of different materials was observed by measuring the efficiency of photocatalytic transformation of pATP to p,p′-dimercaptoazobenzene (DMAB). The photocatalytic reactions were performed at 20 °C and initiated by irradiation with a laser ($\lambda = 633$ nm). On the basis of SERS spectra shown in Fig. 6D, the authors found that hot electrons formed on the surface of unmodified Au NPs can successfully initiate photo-conversion of pATP (Raman peaks at 1000, 1080, and 1178 cm^{-1}) to DMAB (Raman peaks at ca. 1140, 1392, and 1445 cm^{-1}). High efficiency of pATP photo-conversion was also observed for Au NPs covered with a thin shell of TiO_2. As depicted in Fig. 5E, the intensity of the Raman signals typical of DMAB relative to that characteristic of pATP, calculated from in situ SERS spectra recorded during the reaction with the use of the unmodified Au NPs and Au NPs covered with TiO_2, were comparable. Interestingly, significant decrease in the efficiency of photocatalytic transformation of pATP to DMAB was observed for Au NPs covered with a thin layer of SiO_2 or Pd (Fig. 6E). In view of these observations, the authors established that the hot electrons can be transferred more efficiently within the TiO_2 shell than through the shells composed of Pd or SiO_2. Additional in situ SERS studies with the use of Au NPs covered with various thicknesses of Pd or TiO_2 shells allowed estimation of the distance at which the hot electrons can diffuse efficiently through the model semiconductor and the model metal. As depicted in Fig. 6F, the diffusion length of the hot electrons within the palladium shell was

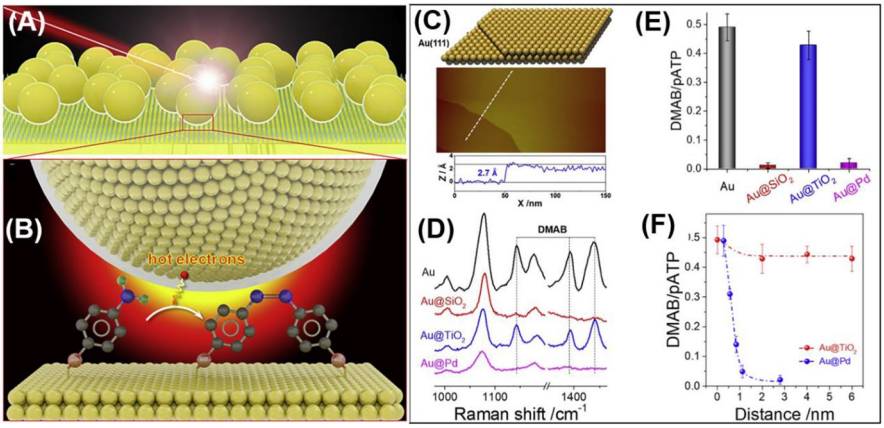

Fig. 6 **A**, **B** Schematic illustration of in situ SERS study on the interfacial transmission of hot electrons using the photocatalytic conversion of pATP to DMAB as a probe reaction. **C** schematic and scanning tunneling microscopy (STM) image of the Au(111) single-crystal surface. The STM image was obtained using a Pt–Ir tip with a dimension of 150×300 nm^2. The bottom panel shows the height profiles corresponding to the white dashed line in the STM image. **D** SERS spectra of the conversion of pATP adsorbed on Au (111) catalyzed by different core–shell nanoparticles. Excitation laser, 633 nm; laser power, 0.1 mW; and exposure time, 10 s. **E** Raman intensity of DMAB relative to pATP for different nanostructures shown in **D**. **F** Raman intensity of DMAB relative to pATP as a function of the shell thickness for Au@TiO_2 and Au@Pd interfaces. (Copyright with the authors permission [47])

much shorter than that observed for the shell composed of titanium dioxide, such a sub-nm special resolution for hot electron diffusion in TiO_2 and Pd by changing the thickness of the TiO_2 and Pd shells.

Another example is related to application of in situ tip-enhanced Raman spectroscopy (TERS) for investigation of the role of reactive arrangement (i.e., orientation and surface coverage) of 4-nitrothiophenol (4-NTP) molecules on Au(111) single crystal in photocatalytic coupling of 4-NTP to p,p′-dimercaptoazobenzene (DMAB) [48]. The different reactive arrangements of 4-NTP species were obtained by using two various experimental protocols: (1) drop-cast method which allowed obtaining of self-assembled monolayer of 4-NTP characterized by low contribution of well-ordered 4-NTP domains (ca. $7.8 \pm 1.0\%$) and (2) immersion protocol that enabled construction of self-assembled monolayer of 4-NTP characterized by high contribution of well-ordered 4-NTP domains (ca. $74.3 \pm 5.5\%$). All TERS measurements were performed with a top-illumination TERS setup combining a scanning tunneling microscope (STM) with a Raman spectrometer (Fig. 7A). A He–Ne laser ($\lambda = 632.8$ nm; Spectra-Physics, Newport, Germany) was used as the excitation source. On the basis of high-resolution in situ 2D TERS imaging of the reaction on the Au(111) crystal, the authors found that DMAB product was identified on almost the whole surface of the drop-cast sample, but some negligible regions containing unreacted 4-NTP substrate were also noticeable (Fig. 7Ba). This observation was further confirmed by results obtained from analysis of six TERS spectra from selected locations where DMAB (P1–P3) and unreacted substrate (P4–P6) were identified. As shown in Fig. 7Bb, Raman signals typical of DMAB (peaks at

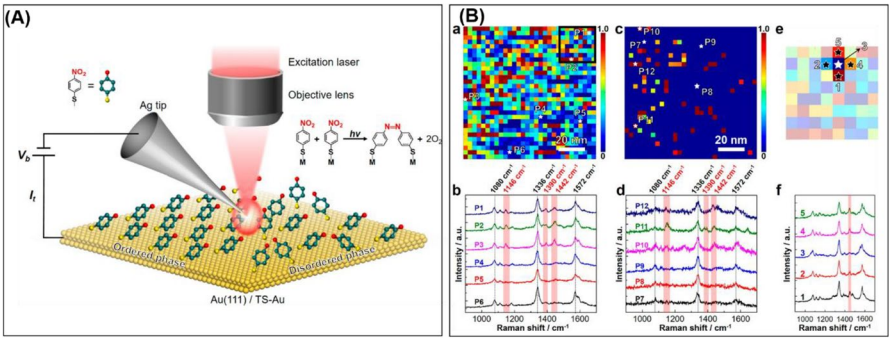

Fig. 7 **A** Schematic diagram of the STM-TERS setup used in this study to investigate reactive arrangement in photocatalytic coupling of 4-NTP → DMAB on polycrystalline and single-crystal Au surfaces; **B** high-resolution TERS images of I_{1442}/I_{1080} ratio measured on samples prepared via **a** drop-cast and **c** immersion protocols on single-crystal Au(111) surfaces. Step size = 3.3 nm. Spectrum integration time = 1 s. **b**, **d** TERS spectra measured at the locations P1–P12 marked in **a**, **c**. **e** Zoomed-in TERS image of the region marked in **a**. Five pixels labeled as 1–5 are highlighted. **f** TERS spectra measured at the pixels labeled in **e**. (Copyright with the authors permission [48])

ca. 1146, 1390, and 1442 cm^{-1}) were found only in spectra from locations P1–P3. In contrast to the drop-cast sample, very low efficiency of 4-NTP photo-conversion was found for the sample obtained by the immersion protocol. In this case, the DMAB product was formed only in several isolated locations (Fig. 7Bc, d). In view of these observations, the authors established that the close-packed molecular arrangement of 4-NTP substrate on the surface of the sample prepared by the immersion method significantly diminished the efficiency of photocatalytic transformation of the substrate to the product. This conclusion was further supported by results obtained from analysis of a zoomed-in TERS image of the selected region of the drop-cast sample (Fig. 7Be). This TERS image, characterized by spatial resolution of ca. 3 nm, indicated that DMAB was formed at all marked positions except position 3, where steric hindrance inhibited photocatalytic conversion of 4-NTP to DMAB (Fig. 7Bf).

2.2.2 In situ Raman Spectroscopy for Investigating Photocatalysis in Liquid Phase

As far as recent in situ Raman studies are concerned, it is important to underline that Rößler et al. [49] developed a new homemade glass reactor that allows in situ monitoring of photocatalytic processes with the use of Raman spectroscopy (Fig. 8A). The reactor was made of glass and composed of a customized Schlenk tube surrounded by 3D-printed illumination units (12 high-power LEDs, Nichia NCSG219B-V1, peak wavelength 520 nm, FWHM 30 nm). The reaction was monitored with the use of a short-focus immersion probe with a sapphire tip mounted in the photo-reactor with GL screw fittings (Bohlender, Grünsfeld, Germany). In situ Raman spectra were collected with the use of an RXN2 spectrometer (Kaiser Optical Systems, Lille, France) equipped with a laser source (785 nm). The new reactor enabled recording of Raman spectra with a temporal resolution of about one minute, i.e., much higher than that available for other offline sampling analyses. It shows

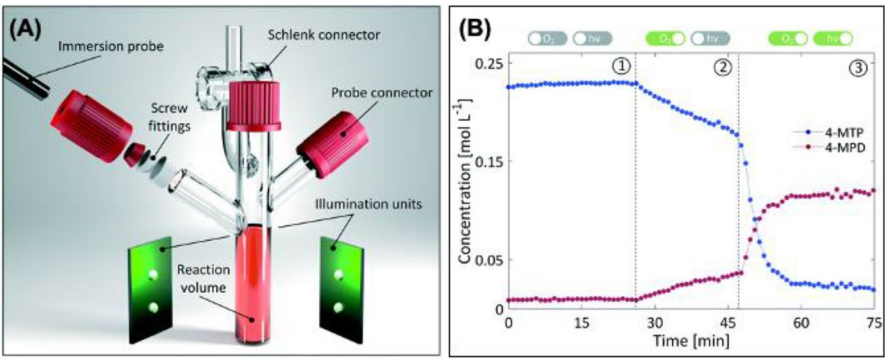

Fig. 8 **A** Representation of the developed setup for studying photocatalytic reaction kinetics. The setup allows simultaneous LED irradiation and in situ monitoring by various analytical technologies (e.g., Raman spectroscopy); **B** evaluation of the concentration–time course for 4-MTP (blue) and 4-MPD (red) by a chemometric indirect hard model (IHM) that resolves the response to the applied reaction conditions. (Copyright with the authors permission [49])

great advantage of the new in situ reactor for monitoring of fast photocatalytic processes which reach equilibrium state in several minutes. As an example, the authors described studies on photo-oxidation of 4-methoxythiophenol (4-MTP) to bis(4-methoxyphenyl)disulfide (4-MPD) catalyzed by eosin Y (EY). The authors found that the oxidation reaction may proceed under dark conditions, but its efficiency is greatly accelerated upon exposure to green LED light. As depicted in Fig. 8B, the concentration of 4-MTD (estimated from in situ Raman spectra by a chemometric indirect hard model) increased immediately upon LED irradiation at the expense of 4-MTP. Detailed kinetics studies allowed estimation of the reaction rate constants. It was established that the photocatalytic reaction was ca. 16 times faster than the reaction under dark conditions (reaction rate constants of 0.013 min^{-1} vs. 0.21 min^{-1}, respectively). This study was significantly affected by excitation light-induced fluorescence problems, and care had to be taken to minimize such interference.

2.3 In situ Electron Paramagnetic Resonance (EPR) Spectroscopy

EPR spectroscopy has been widely used in photocatalysis for monitoring charge carrier trapping, recombination, and transfer as well as for identification of radicals and reactive oxygen species (ROS) [50]. The low frequency of the electromagnetic radiation used for the spin resonance of electrons assures no interference from the frequency of the light, which allows measuring the EPR spectra, in an in situ manner, under irradiation and in dark conditions. Since the lifetime of radicals is usually very short, the detection of such species is often performed in the presence of spin traps that selectively react with a given radical to form a more stable adduct [51]. For example, Zhang et al. [52] used in situ EPR spectroscopy to confirm the formation of hydrogen atoms as an intermediate product during the photocatalytic H_2 production from water over the ternary Pt_1@CNQDs/CNS catalyst (Pt_1 = single platinum atom, CNS = carbon nitride nanosheets, CNQDs = carbon nitride quantum

dots) by using 5,5-dimethyl-1-pyrroline-N-oxide (DMPO) as spin trap. EPR spectra were recorded using the X band on a Bruker E500 spectrometer. The photocatalytic reaction was performed in a top-down illumination reactor using a Xe lamp with a UV cut filter (400 nm $< \lambda <$ 780 nm). Before the measurements, 15 mg of the photocatalyst was added to 150 mL aqueous solution of triethanolamine (10%) as an electron donor and purged with nitrogen gas to remove the dissolved air. As depicted in Fig. 9A, the spin adduct was observed immediately after 20 s of visible light irradiation (nine signal peaks), indicating that H atoms formed as an intermediate during the reaction. By comparing the intensity of the EPR signal, the signal observed in the presence of Pt-containing photocatalysts was much lower than that observed for Pt-free samples, suggesting that the reduction of protons takes place in carbon nitride quantum dots (CNQDs) in the Pt_1@CNQDs/CNS system, while the recombination of H atoms into H_2 takes place on single platinum atoms (Pt_1). In situ EPR technique with DMPO as spin trap was also used by Park et al. [53] to detect the methyl radical ($CH_3^{\cdot}$) as one of the main intermediate products formed during the photocatalytic conversion of CO_2 and water into C_1 to C_3 hydrocarbons over CdS/(Cu/titanate nanotubes). More examples on the application of in situ EPR with the use of a spin trap in photocatalysis can be found elsewhere [54, 55].

As far as application of in situ EPR spectroscopy in photocatalysis is concerned, it is important to underline that this technique also allows for direct observation and monitoring of the paramagnetic active species during photocatalytic processes. For example, Zhang et al. [56] used in situ EPR spectroscopy to confirm the formation of Cu^+ as active species in CuSA-TiO_2 (SA = single atom) during the photocatalytic hydrogen evolution reaction. EPR spectra were recorded at room temperature on a Bruker EMXnano spectrometer. The photocatalytic reaction was performed in a multichannel photothermal reactor (PCX-50C, Perfect Light Ltd.) using a Xe lamp as a simulated solar light source. Before the measurements, 20 mg of the photocatalyst was added to 120 mL of H_2O/methanol mixture (vol. ratio = 1:2) and evacuated under vacuum to remove the dissolved air. The authors revealed that the EPR signal typical of Cu^{2+} ions significantly decreased during the reaction and was restored after exposure to air (Fig. 9B), suggesting the reduction of the Cu^{2+} to EPR-silent

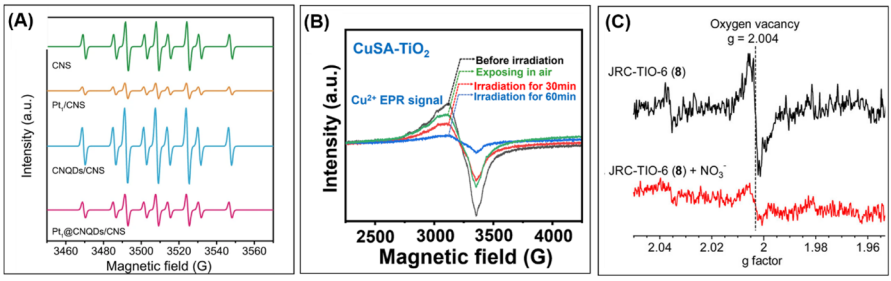

Fig. 9 **A** Deconvolution of experimental EPR signals of DMPO spin adducts generated under irradiation of a 300-W Xe lamp ($\lambda > 400$ nm) for the CNS, Pt_1@CNS, CNQDs/CNS, and Pt_1@CNQDs/CNS. **B** In situ electron paramagnetic resonance spectra of CuSA-TiO_2 with various states. **C** ESR spectra measured at 77 K for JRC-TIO-6 (8) (black trace) and the sample after adsorption of NO_3^- (red trace). (Copyright with the authors permission [28, 51, 53]

Cu^+ species by photogenerated electrons formed in TiO_2, resulting in very efficient production of hydrogen over CuSA-TiO_2 catalyst.

EPR spectroscopy has also been recognized as a very powerful tool to investigate the role of defects in photocatalysis [51]. For example, Hirakawa et al. [27] used in situ EPR spectroscopy to confirm the electron transfer from oxygen vacancies in TiO_2 [JRC-TIO-6 (8)] to the adsorbed NO_3^- species during the selective NO_3^--to-NH_3 reduction under UV light ($\lambda > 300$ nm) in the presence of formic acid (HCOOH) as an electron donor. EPR spectra were recorded on a Bruker EMX-10/12 spectrometer. Before the measurement, 50 mg of the parent catalyst or the catalyst containing NO_3^- species adsorbed on its surface was placed in a quartz tube and evacuated for 4 h. EPR measurements were performed at 77 K. After exposure of TiO_2 photocatalyst to nitrates, the EPR signal typical of unpaired electrons of oxygen vacancies was significantly reduced (Fig. 9C), confirming that surface defects are associated with NO_3^- through electron transfer from Ti^{3+} to NO_3^-, and behaves as a reduction site for NO_3^-. The important role of defect sites during the photocatalytic NH_3 production via N_2 fixation using water was also reported by Shiraishi et al. [57]. The authors show that the signal assigned to the unpaired electrons of the Bi (II) sites in bismuth oxychloride (BiOCl) decreases upon N_2 injection, confirming the electron transfer from Bi (II) to N_2 and the formation of Bi (III) species. Although EPR is extremely sensitive, the measurements are often performed in the presence of a spin trap and/or at low temperature (below 77 K) in order to improve detection of the highly reactive species with unpaired electrons. This is particularly important to monitor charge carriers in photocatalysts where room-temperature measurements are commonly impossible due to fast recombination. Due to these specific drawbacks, the application of EPR in photocatalysis is still scarce under *operando* photocatalytic conditions.

2.4 In situ XAS

X-ray absorption spectroscopy represents a powerful technique to investigate structural and electronic configuration of metal sites in nanostructured and bulk catalysts [58, 59]. The XAS spectrum is traditionally divided into two parts: X-ray absorption near edge structure (XANES) and extended X-ray absorption fine structure (EXAFS). The XANES region allows probing of variation in the oxidation state, density of unoccupied stats, and chemical bond hybridization, while EXAFS is more sensitive to bond lengths and the coordination environment. Compared to the other techniques (IR, Raman), XAS presents advantages in both surface and bulk sensitivities. XAS is most frequently used in transmission mode where the adsorption coefficient μ(E) is registered as a difference in the X-ray flux before and after it passes through the sample in a certain energy range around the absorbing threshold; however, it is highly dependent on the homogeneity and thickness of the sample. Thus, for photocatalytic application, XAS acquisition is more frequently performed via X-ray fluorescence which allows signal registration in high-resolution mode [i.e., high-energy-resolution fluorescence detection-X-ray absorption spectroscopy (HERFD-XAS)] [60]. In photocatalytic applications, *operando* XAS (more details

in the *operando* section) is mostly employed to shed light on the active site's oxidation state upon reaction conditions, while in some cases, it allows retrieval of valuable information about their structural evolution. XAS has been extensively used in recent years for in situ studies of photocatalysis in order to unravel the possible modification of photocatalyst after reaction [61, 62]. In this part, we consider the recent work dedicated to CO_2 photoreduction over pretreated Cu/TiO_2 catalyst (under air or H_2) [21]. Cu K-edge XANES and EXAFS in fluorescence mode were employed to determine the oxidation state and structural differences and elucidate the changes of Cu speciation in Cu/Ti(air) and Cu/Ti(H_2) samples. A quartz tube reactor cell firstly reported by Zhao et al. [63] for catalytic study was adopted for XAS and employed in this work. The sample was coated on a glass slide as a thin film, loaded on a stainless-steel holder, and then placed inside a quartz tube (Fig. 10A). The UV light and X-ray fluorescence propagation was ensured by making a circular hole and taping it with Teflon film. At the two ends of the quartz tube, the valves were sealed with a Kapton film. IR and mercury vapor UV lamps were used as a sample heater and a light source, respectively. The experiment was carried out at beamline 10D

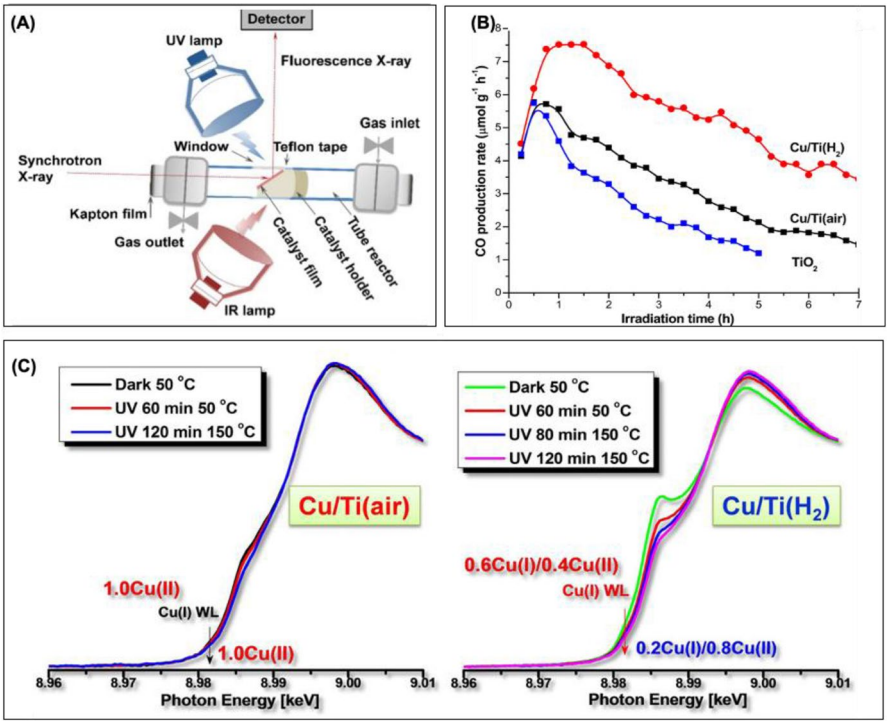

Fig. 10 **A** Experimental setup based on a quartz tube reactor allowing in situ XAS measurements, employed for similar catalyst in pellet form under CO_2 photoreduction conditions. **B** Rate of CO production from CO_2 photoreduction with H_2O vapor over TiO_2, Cu/Ti(air), and Cu/Ti(H_2) under UV–Vis irradiation. (C) In situ XANES spectra for Cu/Ti(air) and Cu/Ti(H_2) in dark at 50 °C and under different conditions of UV irradiations. (Copyright with the authors permission [21])

at the Advanced Photon Source (APS) at Argonne National Laboratory. It was found that the post-treated sample at 200 °C under H_2 (Cu/Ti(H_2)) exhibits more than 50% higher activity for CO_2 photoreduction than the air-calcined one (Cu/Ti(air)) (Fig. 10B). This is explained by the higher population of Cu^+ species as the active sites in Cu/Ti(H_2). In dark (Fig. 10C), the Cu/Ti(air) surface is dominated by Cu^{2+} with an insignificant number of Cu^+, while the pre-reduced Cu/Ti(H_2) sample is characterized by significantly more intensive Cu^+ ions with a Cu^+/Cu^{2+} ratio of about 60:40. Under UV irradiation at 150 °C (Fig. 10C), no significant difference was observed in the copper speciation of Cu/Ti(air), while further decrease of the Cu^+ component was detected in Cu/Ti(H_2) with an equimolar ratio of Cu^+/Cu^{2+} after 120 min of reaction. The authors demonstrated that the origin of Cu/Ti(H_2) deactivation is related to substantial oxidation of Cu^+ to Cu^{2+} that occurs during the reaction. In the same study, in situ DRIFTS was also used to investigate the CO_2 photoreduction over pretreated Cu/TiO_2 catalyst, and similar results were obtained (see the in situ FTIR section).

3 *Operando* Techniques in Photocatalysis

To avoid a lengthy discussion, we present herein the most commonly used *operando* techniques in photocatalysis such as infrared spectroscopy (DRIFTS, ATR-IR, SSITKA) [4, 64–70], Raman [71], and X-ray absorption spectroscopy (EXAFS and XANES) [72–74], including some examples provided to better understand the reaction mechanisms.

3.1 *Operando* FTIR Spectroscopy in Photocatalysis

Operando FTIR is a powerful technique to track the variations in the gas phase or on a catalyst's surface at seconds timescale with high sensitivity and relatively rapid response. In photocatalysis, a homogeneous irradiation of the photocatalysts is very difficult. Consequently, the possible contribution of chemical reaction in the dark regions of the catalyst may complicate interpretation of the results. To overcome this problem, many reactors have been developed or modified for FTIR *operando* studies in photocatalysis [67–69, 75]. The FTIR reactor must respond to a number of criteria, such as (1) homogeneous illumination of the photocatalyst, (2) minimum leaching of photocatalysts in case of reaction in liquid phase, (3) reduced dead volume (i.e., the residual space between the photoreactor windows and the sample), and (4) accurate control of the reaction parameters (e.g., contact time, temperature, irradiation intensity, reaction composition). Here, the use of the *operando* FTIR technique, essentially in transmission mode which allows one to simultaneously and quantitatively analyze the gas phase and the catalyst surface under the reaction conditions, will be illustrated by the most recent and conclusive case studies. Each case study will present a brief description of the proper homemade/commercial reaction cells followed by the identification of the active sites and/or the reaction intermediates to unravel the reaction mechanism.

3.1.1 *Operando* FTIR for Investigating Photocatalytic Reactions in Gas Phase

Despite the limitation of *operando* DRIFTS, this technique has been extensively used to study the photocatalytic reaction in gas phase [64, 65, 75–77]. For the sake of brevity, only the first we know of and a recent example are presented here. Wu's work in 2006 [75] reported the *operando* study of the photocatalytic reaction of NO on TiO_2 and TiO_2-supported Cu, V, and Cr oxide catalysts in a Harrick HVC-DRP-1 cell. The DRIFT spectra show that NO adsorbs titrating surface hydroxyl, peroxo, or M=O species along with the formation of nitrosyls on oxide sites. DRIFTS shows that bidentate nitrites oxidize to monodentate or bidentate nitrates upon photoexcitation, which appears associated with the generation of superoxo species. A recent *operando* DRIFTS analysis addresses the photo-assisted hydrogenation of CO_2 over Au/TiO_2 under visible light at different temperatures from 150 to 500 °C [76]. In the experimental setup, 10 mg of the sieved catalyst (63–125 µm) was packed into the commercial Praying Mantis reactor. The reaction mixture of CO_2 (1 cc/min) and H_2 (4 cc/min) in argon (25 cc/min) and the gas products were monitored with a mass spectrometer. The irradiation was provided by external green (520 nm, 250.1 mW/cm^2) and blue (445 nm, 320 mW/cm^2) LED lights via an optical guide placed at the front quartz window of the reactor. Steady-state isotopic transient kinetic analysis (SSITKA) and kinetic isotope effect (KIE) were also performed to obtain the transient condition by switching to labeled molecules (e.g., $^{13}CO_2$ and D_2) at the steady state of the reaction. The results show that the highest CO_2 conversion into CO over Au/TiO_2 is obtained at 500 °C under green light (Fig. 11A). The main reaction pathway is the direct dissociation of CO_2 at the oxygen vacancy (VO) of Au/TiO_2 via a redox mechanism. When switching from $^{12}CO_2$ to $^{13}CO_2$ both in dark and under visible light, the IR peaks of surface bicarbonates (HCO_3*, 1440 cm^{-1}) and carbonates (CO_3*, 1560 cm^{-1}) gradually decrease, while that of formates (HCOO*, 2955 cm^{-1}) remains unchanged. A shift to lower wave number of CO_3* and HCO_3* IR peaks, without any changes in the HCOO* band, was also observed after exchange with $^{13}CO_2$ in the absence of H_2. Furthermore, no correlation was found between the surface residual time of CO_3* and HCO_3* surface species and that of produced CO. The former species were also not sensitive to the intensity of the incident light. This confirms that all of HCOO*, CO_3*, and HCO_3* surface species are spectators. The labelled CO_2 experiments conducted on a clean (without carbon species) and reduced Au/TiO_{2-x} sample (with oxygen vacancies) in the absence of H_2 at 200 °C showed the shift to lower wavelength of two peaks at 2176 and 2077 cm^{-1} assigned to ^{12}CO adsorbed on Ti^{4+} and $Au^{\delta-}$ sites of Au/TiO_{2-x} (Fig. 11C). Furthermore, the H/D kinetic isotope effects (KIE) measured in dark and under visible irradiation in the range of 200–400 °C were smaller than one in all cases (Fig. 11B). This is unambiguous evidence of dissociative adsorption of CO_2 on the Au/TiO_{2-x} which rules out involvement of the bond formation/cleavage with H/D as elementary steps.

Knowing that transmission IR is the technique of choice to simultaneously analyze the surface and gas phases during *operando* studies, some examples are discussed in details in this part. In 2009, the photo-oxidation of acetone over TiO_2-ZrO_2 thin films was studied using the *operando* FTIR technique [68] using a modified version of the IR transmission in situ cell designed by M.A. Anderson's

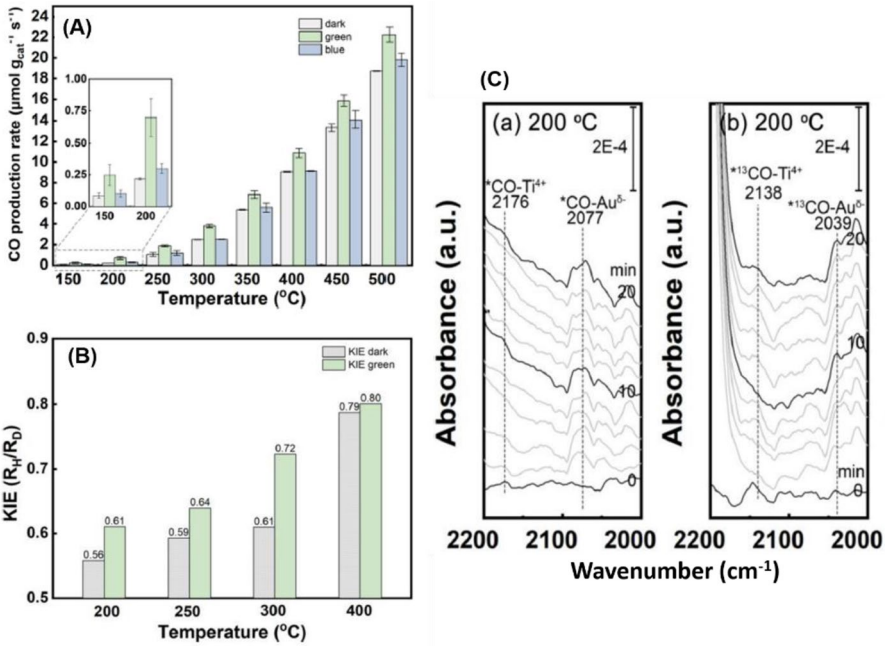

Fig. 11 **A** The CO production rates over Au/TiO_2 photocatalyst during photo-assisted CO_2 hydrogenation at temperature ranging from 150 to 500 °C under dark, green light, and blue light irradiation. The inset is the magnification of columns at 150 and 200 °C. **B** H_2/D_2 kinetic isotope effects of reverse water-gas shift (RWGS) reaction under dark or green light irradiation at different temperatures. **C** Time-resolved DRIFT spectra of CO_2 interaction with reduced Au/TiO_{2-x} in flowing Ar with the absence of H_2: **a** $^{12}CO_2$, **b** $^{13}CO_2$ at 200 °C. (Copyright with the authors permission [76])

group in 2004 [78]. In the new version, the contact time between the gas and the photocatalysts was maximized by flowing the gas on the two sides of catalyst (Fig. 12A). The cell was equipped with quartz and BaF_2 windows transparent to UV–Vis and IR irradiations, respectively. In the experimental setup, the Si wafer coated with the photocatalytic thin films was placed in the reactor and then equilibrated with acetone vapor (0.5 µL of liquid) for 40 min prior to the reaction with a total flow rate of 75 cm^3/min. Then, the films were irradiated in air with four UV lamps externally placed in an aluminum frame. The total volume of the system was about 0.55 L. The FTIR spectrum were simultaneously recorded for the catalyst surface (200 scans, 4 cm^{-1} of resolution) and the gas phase (64 scans, 1 cm^{-1} of resolution), noting that interferences with the surface bands were not significant.

The obtained results indicate that the TiO_2(90%)-ZrO_2(10%) mixture exhibits the highest conversion rate for acetone photodegradation under UV light as compared to $Ti_{0.9}Zr0_{0.1}O_2$ mixed oxide and TiO_2. The CO_2, H_2O, and minor amount of CO are the only products detected in the gas phase over the three samples. It was concluded from surface analysis that the presence of Zr centers seems to promote the formation of formate beside formaldehyde as intermediates, while

Fig. 12 **A** Picture and cross-sectional view of the transmission cell used to test the photocatalytic activity of the thin films showing the path followed by the gas stream inside this device and the materials used for manufacturing the different components. **B** **a** FTIR spectra in the 2000–1150-cm^{-1} range of the ZrO_2(10%)-TiO_2(90%) sample contacted with acetone vapor (0.5 µL of liquid) and subsequently UV-irradiated for increasing periods of time as indicated in the graphs. Spectra of the photocatalytic coating before acetone adsorption have been subtracted in order to highlight the bands corresponding to surface species and variation of the normalized intensities of adsorbed species; **b** evolution of acetone (squares), formate (up-triangles), aldehydes (down-triangles), CO_2 production (circles), and photogenerated electrons (diamonds) detected during UV irradiation of the ZO_2(10%)-TiO_2(90%) sample. The latter are represented by plotting the increment in background intensity at ca. 1020 cm^{-1} as a function of irradiation time. Vertical lines mark the different stages of the photocatalytic processes. **C** Evolution of adsorbed **a** toluene and **b** methylcyclohexane (MCH), CO_2, and intermediates during UV irradiation over the TiO-ZrO_2 mechanical mixture. (Copyright with permission from Refs. [68, 78])

formaldehyde is the only surface species detected on the TiO_2 film. The reaction pathway over TiO_2(90%)-ZrO_2(10%) mixture contains three main steps (Fig. 12B): (1) the rapid acetone adsorption equilibrium in dark, (2) the transformation of the adsorbed acetone to formaldehyde and formate as intermediate surface species upon UV irradiation, and the (3) oxidation of formaldehyde which is quicker than that of formate into CO_2. This is confirmed by the evolution of the surface species and their integrated intensity during the photocatalytic reaction (Fig. 12Ba–b), which shows the progressive decrease of IR acetone bands (1703, 1371, 1241 cm^{-1}) after turning on the lamp. Then, formate and formaldehyde species appeared at 1569 (broad) and 1744 cm^{-1}, respectively. However, after 120 min of irradiation, formate species were completely removed, and a new band appeared at 1447 cm^{-1} due to the formation of bicarbonates on catalyst surface. Two years later, the same IR transmission in situ cell was used to understand the effect of the chemical structure of the pollutants methylcyclohexane (MCH) and toluene on the photocatalytic activity of TiO_2-ZrO_2 thin films [64]. It was shown that the aromatic character of toluene plays a key role in the catalyst deactivation, while this process was inhibited during the photo-oxidation of cyclohexane. The deactivation process was correlated to the formation of benzoate complexes strongly adsorbed on the catalyst's surface, which block the access to the active sites and the regeneration of hydroxyl groups (deduced from the intensity of the OH band at 3690 cm^{-1}) (Fig. 12Ca). By contrast, no deactivation was observed during the photo-oxidation of MCH due to the weak interaction of the reaction intermediates (i.e., cyclohexanone) with the catalyst surface and the full regeneration of OH groups (Fig. 12Cb). It should be noted that the configuration used in both studies, in which the Si wafers were coated with the photocatalytic thin films, ensures full illumination of the sample with, however, a reduced signal intensity due to the low mass of the photocatalyst and low-efficiency flow distribution due to the preferential paths.

Since 2012 and successively, a new *operando* IR reactor [79] has been reported by El-Roz et al. to study photocatalysis reaction for air purification (e.g., photo-oxidation of methanol, CO_2 photoreduction, photo-assisted selective catalytic reduction of NO_x) [4, 33, 80–83]. In the photocatalytic experiments (Scheme 3), the light irradiation was delivered by a UV–Vis lamp connected to an optical fiber light guide placed at the entrance of the cell to ensure a homogeneous irradiation

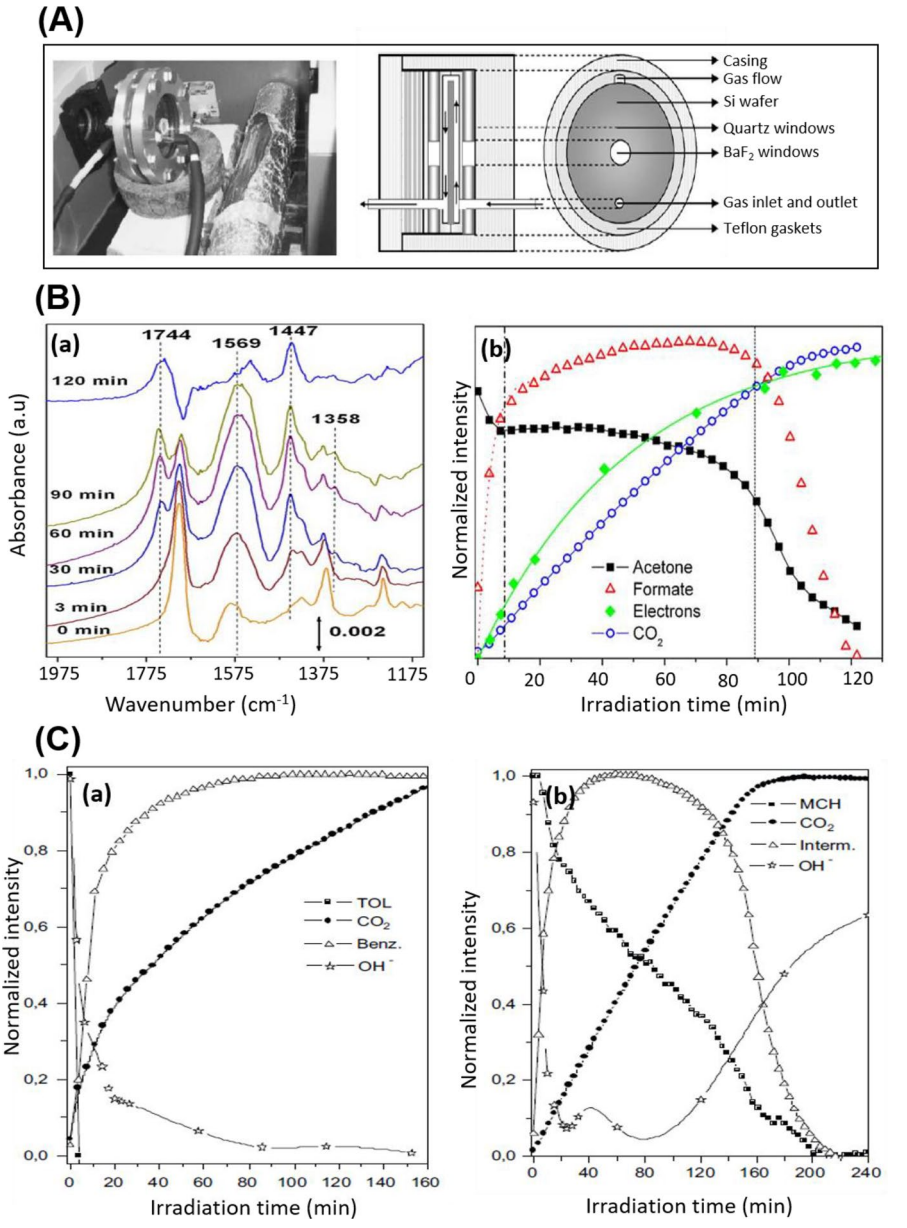

of the pellet (self-supported pellets of ~ 20 mg and 2 cm^2). This reactor presents several advantages: (1) the thin pellet-shaped sample which limits the mass loss and ensures a homogeneous illumination of catalyst; (2) the control of irradiation parameters (intensity, mono- or polychromatic, UV or visible light, etc.) without replacement of the photoreactor; (3) the reduced dead volume ~ 0.4 mL; (4) the online analysis techniques (IR, GC, MS, etc.) providing high-precision data, and

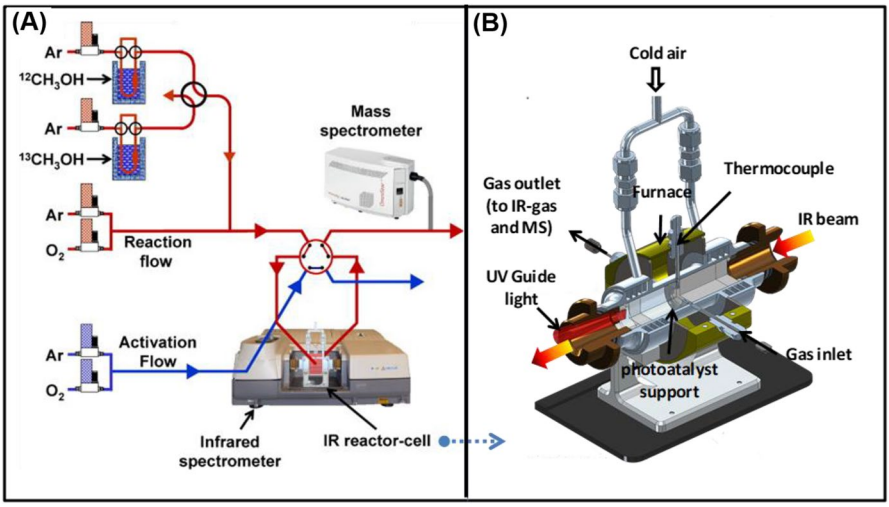

Scheme 3 *Operando* setup (**A**) and sandwich reactor IR cell (**B**) modified by El Roz et al. for studying UV–Vis photocatalysis. (Copyright with the authors permission [80])

(5) the accurate control of the reaction temperature (25–600 °C), the gas composition/concentrations (from few ppm to a few percent), and the gas flow (1–50 cm^3/min). In what follows, some examples on *operando* FTIR photocatalytic studies conducted by El-Roz group's using the FTIR reactor cell described above are presented.

The photocatalytic oxidation of methanol over TiO_2-based catalysts has been extensively studied by El-Roz et al. as a model reaction. FTIR *operando* spectroscopy coupled with SSITKA was used to clarify the role of formate species during methanol photo-oxidation over hierarchical TiO_2 (TiO_2-L) [4]. In the experimental setup, the self-supported wafers (20 mg) were exposed to the reaction mixture of 400–1200 ppm MeOH and 20% O_2 in argon with 25-cm^3/min total flow. The UV irradiation was provided by a Xe–Hg lamp (200 W, $I_0 = 2$ mW/cm^2). The photocatalytic reaction was simultaneously monitored by IR spectroscopy coupled with mass spectrometry (MS). It was concluded that only a minor part of formate species are involved in the reaction and that most of them are spectators, while methoxy groups are the first intermediates during methanol photo-oxidation. This was confirmed by SSITKA experiments in which the isotopic exchange rate of surface methoxy groups (methoxy ^{12}C 1150 cm^{-1}; methoxy ^{13}C 1090 cm^{-1}) was similar to that of the final gas products, while formate species (formate ^{12}C 1574 and 1366 cm^{-1}; formate ^{13}C 1515 and 1340 cm^{-1}) reacted too slowly, compared to the CO_2 (2400–2200 cm^{-1}) and methyl formate (1800–1600 cm^{-1}) production rate (Fig. 13A, B). Interestingly, the *operando* experiments allow us to highlight the possible sites for the formation of weakly or not active formate species. By plotting the IR band of surface formate species vs. that of the TiOH group at 3720 cm^{-1}, a linear relationship was obtained which highlights the role of hydroxyls on the formation/stabilization of low-activity formate species under UV irradiation (Fig. 13C).

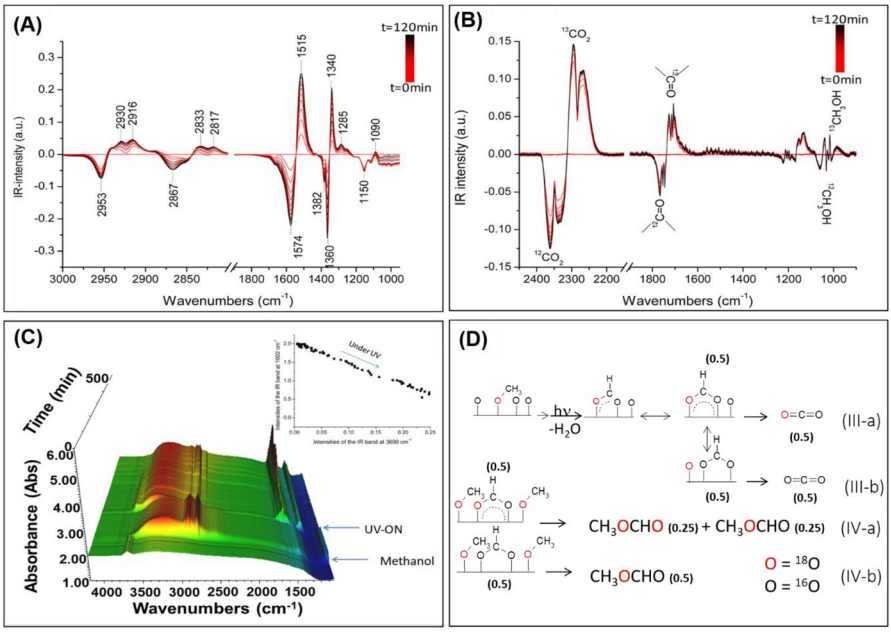

Fig. 13 **A** IR spectra of TiO_2–P25 and **B** the reaction gas phase during a SSITKA experiment for which an initial flow of 1200 ppm of $^{12}CH_3OH$, 20% of oxygen diluted in Ar (total flow = 25 cm^3 min^{-1}) was switched to a similar but labeled ($^{13}CH_3OH$) flow (the spectrum recorded at $t = 0$ was used as background). **C** Evolution of the IR spectra of TiO_2-L during methanol photo-oxidation. Inset: correlation between the IR band areas at 1602 cm^{-1} and 3690 cm^{-1}. **D** Mechanism of the formation of carbon dioxide and methylformate during $CH_3{}^{18}OH$ photo-oxidation. ^{16}O (in black) corresponds to the oxygen coming from the TiO_2 surface (bridged oxygen) and/or molecular oxygen chemisorbed on TiO_2 (oxygen adatom), while ^{18}O (in red) is coming from $CH_3{}^{18}OH$. (Copyright with permission from Refs. [4, 82])

FTIR *operando* spectroscopy has been also used to study the methanol concentration effect on the activity/selectivity of hierarchical TiO_2 (TiO_2-L) during methanol photo-oxidation [82]. It was concluded that the methanol concentration influences greatly the selectivity of TiO_2 during the MeOH photo-oxidation under UV light. At 500 ppm of MeOH, a total conversion and selectivity of MeOH into CO_2 and H_2O were obtained, while they decreased (75% MeOH conversion and 60% CO_2 selectivity) by increasing the MeOH concentration at 1200 ppm due to the formation of a secondary product, i.e. methylformate (MF), in the gas phase. The formation of MF is favored by a high coverage of surface methoxy groups and their further cross-coupling reaction with the neighboring formyl/formate species. All of these results were discussed in details using CD_3OH, $CH_3{}^{18}OH$, and $CH_3OH/{}^{13}CH_3OH$ SSITKA experiments. During the $CH_3{}^{18}OH$ experiments, the formation of 3% labelled CO_2 ($C^{18}O^{18}O$) via ^{18}O-formyl intermediates bridged over ^{18}O surface sites was observed (Fig. 13D). It was suggested that the ^{18}O surface sites originate from the scrambling of formate species on the TiO_2. $C^{16}O_2$, and $CH_3{}^{18}OCH^{16}O$ were the unexpected major products. The difference between the expected statistical value of the intermediate and of the final

products in respect to the experimental values confirms the formate scrambling hypothesis. In the same *operando* study [82], the authors shed light on the shading effect. i.e., inhomogeneous irradiation with the catalyst's depth, on the MeOH photo-oxidation under UV light over three different pellets: (1) a self-supporting pellet of 20 mg (diameter 16 mm, thickness 50–70 µm), (2) a supported pellet of 5 mg on a stainless-steel grid (diameter 6 mm, thickness 50–70 µm), and (3) supported TiO_2 (~ 3 mg) on a KBr window (diameter 16 mm, < 10 µm thickness). A significant activity difference was observed between the three cases, confirming the shading effect, which was at minimum for TiO_2 powder supported on KBr. More recently, Wolski et al. [84]. reported that the nature of the light source (UV vs. visible light) greatly influences the selectivity of MeOH photo-oxidation over the bimetallic Au–Cu–Nb_2O_5 catalyst. Under visible light, both Cu and Au are activated, which promotes the total oxidation of MeOH into CO_2. By contrast, the Cu, Au, and Nb_2O_5 are all excited under UV irradiation, leading to the formation of partial oxidation products such as formaldehyde, methyl formate, and dimethoxymethane. These differences in the reaction pathways were ascertained from the FTIR surface analysis during the reaction: the surface formate species (band at 1583 cm^{-1}) and all intermediates are immediately transformed into CO_2 by changing the light source from UV to visible irradiation, without the formation of other intermediates.

3.1.2 *Operando* FTIR for Investigating Photocatalytic Reactions in Liquid Phase

Since *operando* FTIR in DRIFTS or transmission mode is not suitable for photocatalytic reaction in liquid phase, ATR-FTIR is the most used technique to monitor the catalyst surface in contact with a liquid phase. Very recently, an *operando* ATR-FTIR device was used to study the photocatalytic water splitting over Ga_2O_3-based photocatalysts [$Rh_{0.5}Cr_{1.5}O_3/Ga_2O_3$(Zn)] [85]. The ZnSe was coated with 1 mL of aqueous catalyst slurry (1.6 mg/mL) to form a catalyst film with 0.7 or 4.2 µm of thickness. Then, 0.3 g of distilled water was introduced into the cell under He with 15 cc/min total flow. The UV irradiation was provided by a laser ($\lambda = 263$ nm, power = 110 mW) fixed on the top of the catalyst film with an adjusted spot to match the shape of the catalyst by using a set of optics. During the reaction, the catalyst surface and the gas phase were monitored by ATR-IR and mass spectrometer, respectively. A direct hydroxyl radical formation from the oxygen atoms in H_2O without involving the lattice O atoms of the photocatalysts was proved. Under UV irradiation, the IR spectrum of the photocatalyst film in contact with water shows three bands at 872, 1382, and 978 cm^{-1} (Fig. 13Aa). The two first bands were assigned to the stretching and bending modes of the physically adsorbed H_2O_2, while the third one was attributed to the negatively charged hydroperoxide group, i.e., Ga–OOH^- surrounded by water molecules. These assignments were confirmed by the band shifts observed after isotopic exchange (D_2O and $H_2{}^{18}O$) (Fig. 14Aa–b). It was noted that the frequencies of the stretching and bending modes of O–H in the physically adsorbed H_2O_2 are, respectively, not sensitive to H–D and ^{18}O isotopic exchange (Fig. 14Ac). In addition, only $^{18}O^{18}O$ was detected by mass spectroscopy in the $H_2{}^{18}O$ isotopic exchange. This confirms that the oxygen atoms in H_2O are the

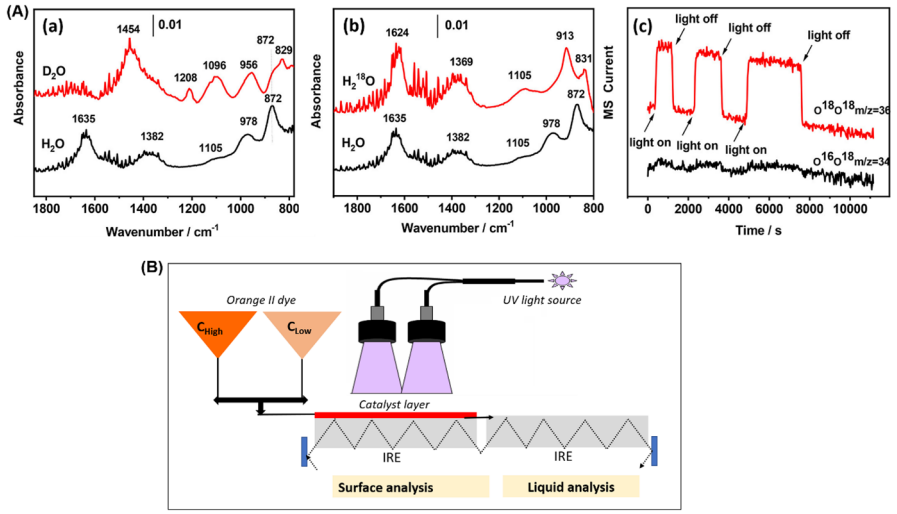

Fig. 14 **A** ATR-FTIR absorption spectra of the 4.2-μm $Rh_{0.5}Cr_{1.5}O_3/Ga_2O_3$(Zn) film in contact with **a** D_2O or H_2O and **b** $H_2{}^{18}O$ or H_2O irradiated by a 263-nm laser with the spectrum taken before the laser irradiation as the background; **c** time courses of MS current for $^{16}O^{18}O$ ($m/z = 34$) and $^{18}O^{18}O$ ($m/z = 36$) involved in the photocatalytic splitting of the $H_2{}^{18}O$ photocatalyst. Three reaction cycles with the irradiation light being chopped on and off are shown. **B** Scheme of the MES-ATR-IR *operando* setup during photodecomposition of Orange II over Au-Fe/TiO_2. (Copyright with the authors permission [85, 86])

sole source of water splitting and that the lattice O atoms in the photocatalysts do not participate to the reaction.

Operando ATR-IR combined with modulation excitation spectroscopy (MES) was also reported and used to study the performance of Au-Fe/TiO_2 nanocomposite during the photodegradation of azo dye (Orange II) under UV and at RT [86]. Catalyst layers were prepared by the deposition/evaporation method on Ge IRE. The Orange II solutions were connected to two ATR-IR reactor cells with and without a catalyst layer in order to simultaneously monitor the catalyst's surface and the liquid phase during the reaction (Fig. 14B). Both surface and liquid spectra were recorded by altering the feeding of two different solutions (Orange II + H_2O + O_2 + UV ↔ H_2O + O_2 + UV) over Au-Fe/TiO_2 with different Au/Fe ratios (0, 1:2, 1:1, and 1:0.5). It was concluded that the increase of Fe loading in Au/TiO_2 leads to slower the adsorption of Orange II and weakens the dye–catalyst interaction, resulting in a fast photodecomposition. By contrast, the stronger adsorption of Orange II on Au/TiO_2seems to suppress its photodecomposition.

3.2 *Operando* Raman Spectroscopy

The *operando* Raman technique is a useful technique to monitor the structural transformation of photocatalysts and to identify the reaction intermediates under real reaction conditions. However, the application of *operando* Raman spectroscopy in photocatalytic reaction is still limited because photocatalysis excitation light may

Fig. 15 **A** Reaction system for the liquid-phase epoxidation and **B** representative Raman spectra during the photocatalytic cyclohexene epoxidation with t-BuOOH over $V_{0.25}Ti_2$/MCM-41 catalyst at 60 °C for 75 min: **a** full spectra; **b** partial spectra in range of 775–930 cm^{-1}. **C** **a** SERS spectra of PATP on TiO_2 IO under the irradiation of a 532-nm laser for 15 min with a time interval of 5 min; **b** evolution of $\nu N=N$ peak recorded with a time interval of 30 s; **c** the logarithm of $(I_t/I_0)1437$ processed using the normalized vibration peak intensity of TiO_2 at 146 cm^{-1} as an internal control; **d** reaction rate constants for the cleavage of C–S, N=N, and C–C bonds under long-time irradiation of a 532-nm laser with a power of 5.0 mW and the corresponding wavenumber deviation collected at different times (inset). (Copyright with permission from Ref. [87, 88])

overwhelm Raman photons. For this reason, *operando* Raman spectroscopy is usually used complementary to IR. To the best of our knowledge, the *operando* Raman spectroscopy is mainly used to monitor photocatalytic reactions in liquid phase. In this section, some case studies are presented where *operando* Raman spectroscopy is used to monitor processes during photocatalytic reactions.

3.2.1 *Operando* Raman Spectroscopy for Investigating Photocatalysis in Liquid Phase

For example, Bañares et al. [87] studied the photocatalytic epoxidation of cyclohexane in the presence of tert-butyl hydroperoxide (t-BuOOH) over V_xTi_y/MCM-41 catalyst under UV light using the real-time NIR-Raman spectroscopy. In the experimental setup (Fig. 15A), the reaction in liquid phase was monitored with a Photonics immersion probe fitted to a PerkinElmer Raman Station 400F system. An NIR filter (cutoff above 750 nm) was used to cancel any residual radiation that might interfere with Raman signals. The Raman spectra were acquired every 10 min with six accumulations of 10 s.

It was shown that the cyclohexene was directly photo-epoxidized over $V_{0.25}Ti_2$/MCM-41 into 1,2-epoxycyclohexane (Raman peak at 784 cm^{-1}) with 100% selectivity (Fig. 15Ba). The presence of an isosbestic point at 800 cm^{-1} between the decreased Raman band of cyclohexene (824 cm^{-1}) and the increased one of epoxide (784 cm^{-1}) indicates the absence of any stable intermediates during the reaction (Fig. 15Bb). In another example, surface-enhanced Raman scattering (SERS) was used to monitor the photo-oxidation of p-aminothiophenol (PATP) on TiO_2 under 532-nm laser irradiation [88]. In the experimental part, the TiO_2 was used as the SERS substrate and the photocatalyst on which the PATP was chemisorbed. The SERS spectra were then collected with an accumulation time of 30 s. The TiO_2 Raman band at 146 cm^{-1} was used as an internal intensity standard due to its stability during the long-time irradiation. The results show that the photodegradation of pATP was initiated by the formation of azo compounds (Fig. 15Ca). Interestingly, the SERS allowed determining the decomposition rate of N=N (1437 cm^{-1}), C–S (1089 cm^{-1}), and C–C (1593 cm^{-1}), which follow a first-order kinetic process with a reaction rate in the range of $2.1–2.7 \times 10^{-3}$ s^{-1} (Fig. 15Cb–d)).

Operando Raman spectroscopy has been recently used to study the photocatalytic hydrogen evolution reaction (HER) over $MoS_{2x}Se_{2(1-x)}$ nanosheets under realistic reaction conditions [89]. In the experimental setup (Fig. 16A), the AM 1.5G illumination (100 mW cm^{-2}) was used as a light source. The laser wavelength was 532 nm with

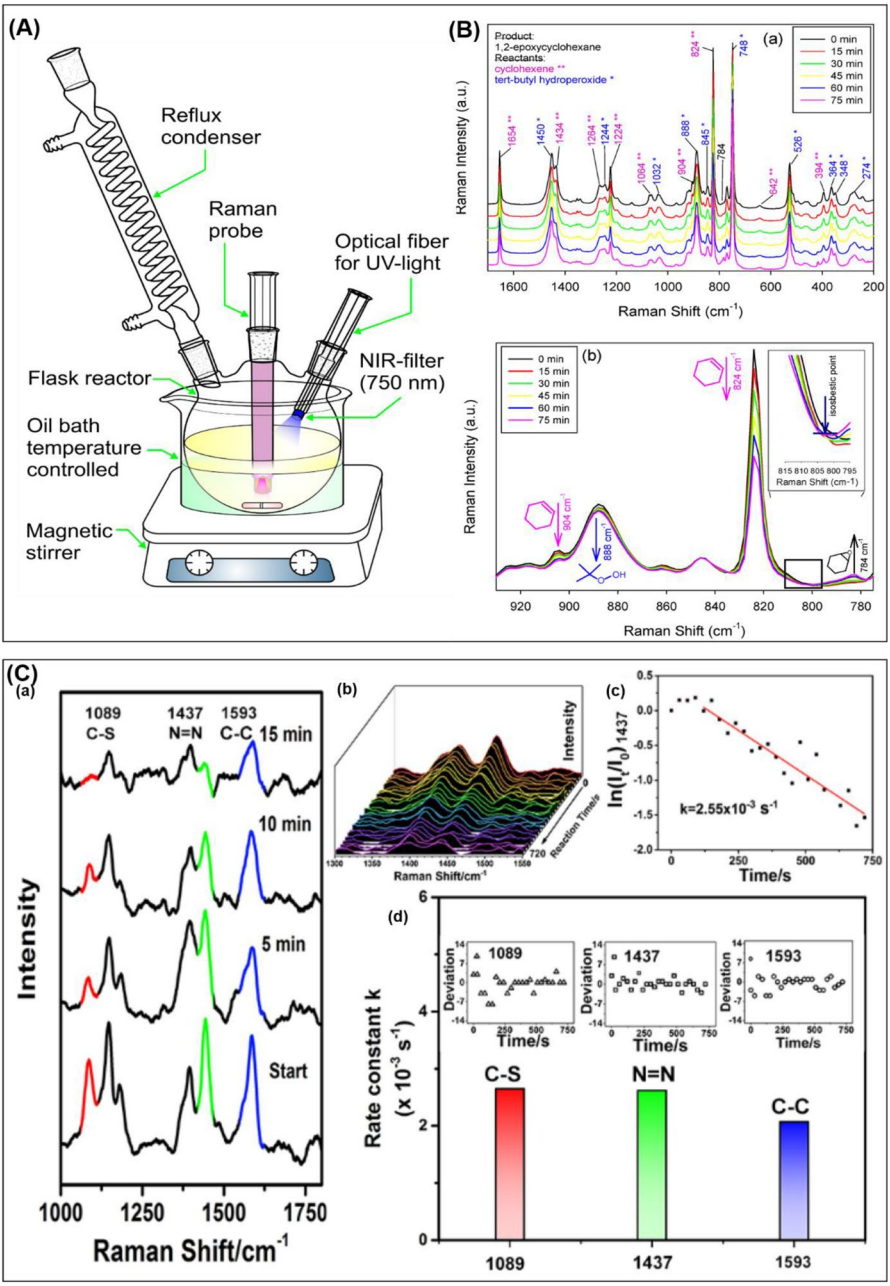

5 mW of light intensity, and the exposure time was 5 s. It has been demonstrated that hydrogen atoms are initially adsorbed on the S and Se active sites to form S–H and Se–H intermediate species followed by its subsequent redox reaction (Fig. 16B). An exponential function relationship was established between the Raman intensity of these

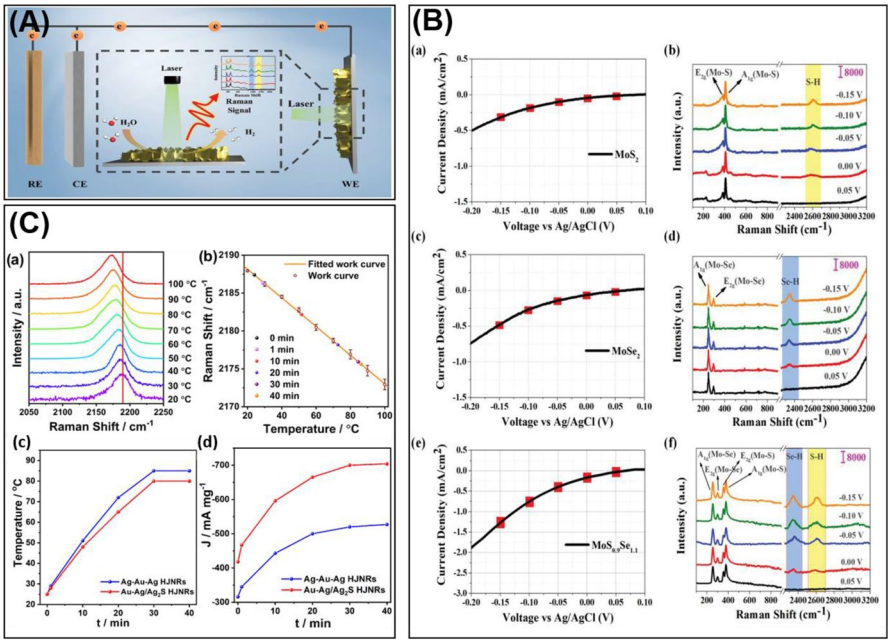

Fig. 16 **A** Schematic of the photoelectrochemical system with linear sweep voltammetry (LSV)-Raman analysis. The measured material is $MoS_{2x}Se_{2(1-x)}$. The reference electrode, counter electrode, and working electrode are termed as RE, CE, and WE, respectively. Evolution of **B** LSV vs. the voltage (0.05, 0.00, −0.05, −0.10, and −0.15 V) and the Raman spectra of the samples **a**, **b** MoS_2, **c**, **d** $MoSe_2$, and **e**, **f** $MoS_{0.9}Se_{1.1}$. **C** **a** SERS spectra of MI on the Au–Ag/Ag_2S HJNRs at different temperatures. **b** Dependence of fitted temperature on the Raman shifts of MI for the Au–Ag/Ag_2S HJNRs. **c** Hot spot temperatures of the Ag–Au–Ag and Au–Ag/Ag_2S HJNRs illuminated for different times; **d** photocatalytic activity of the Ag–Au–Ag and Au–Ag/Ag_2S HJNRs illuminated for different times. (Copyright with permission from Refs. [89, 90])

intermediate species and the number of reactive electrons, which can be used as a guideline to evaluate the hydrogen production performance of the photocatalyst. More recently, Wang et al. [90] designed a simple method to measure the photocatalyst's surface temperature by *operando* Raman spectroscopy using 4-methoxyphenyl isocyanide (MI) as a probe molecule. The νN≡C frequencies of MI adsorbed on the catalyst surface are linearly dependent on temperature (Fig. 16Ca–b). This method was used to unravel the photocatalytic mechanism induced by hot carriers and photothermal effect during the HER over Ag–Au–Ag and Au–Ag/Ag_2S heterojunction nanorods (HJNRs). Although the hot spot temperatures of the Ag–Au–Ag HJNRs are higher than those for the Au–Ag/Ag_2S HJNRs, the latter exhibits higher photocatalytic activity due to the higher contribution of the hot carrier effect (Fig. 16Cc–d).

3.3 *Operando* XAS

In this section, we will report some recent case studies where *operando* XAS has been applied on different photocatalytic reactions, such as methanol photo-reforming

and photocatalytic HER. In the context of cell design, all the aforementioned criteria for an FTIR cell are valid also for *operando* XAS reactors. Among listed criteria—matching between the light illuminated, reaction mixture exposure, and the spectroscopically probed sample volumes—is of particular importance when XAS is used as a probe technique, being sensitive both to the bulk and surface species. The light propagation issue was thoroughly investigated for the most widespread Ti-based photocatalyst in the recent work by Caudillo-Flores et al. [71].

3.3.1 *Operando* XAS for Investigating Photocatalysis in Gas-Phase

In the recent work by Munoz-Batista [72], spatially resolved XAS study of Cu-Ni TiO_2 catalytic bed upon methanol reforming using a micro-beam mode (BM23 beamline, European Synchrotron Radiation Facility [ESRF]) was reported. The cell made of Inconel alloy with high resistance to reducing and oxidizing atmospheres for a wide range of temperatures (25–600 °C) is a modified version of that developed by Agostini et al. [91]. The cell can be separated into two parts: the main body and dome. The heater, thermocouple, sample holder, and gas system are located in the body part, while the dome hosts IR and X-ray windows. The additional window implemented in the cell dome for X-ray fluorescence registration is the main difference in the new version. This upgrade makes the cell suitable for catalysts represented by dilute materials on top of heavy matrix or those with very low metal loading. The powder sample is fixed between two carbon/glass windows, transparent for X-rays with a modified path in range from 1 to 5 mm. The metal grid below the powder (see Fig. 17A) can maximize the interaction between gas flow and catalyst. The lid of the dome equipped with a circular window of KBr and CaF_2 is transparent to IR and UV irradiations. The latter was placed on top of the cell, and the catalytic bed was monitored vertically at the different sample regions upon illumination. A water–methanol liquid mixture was injected into a He carrier gas and delivered to the cell. In situ micro-beam XAS detection was performed in a fluorescence mode.

It was found that in the outermost layer, the copper is present in a fully reduced state in dark and in the presence of methanol. The authors demonstrated that both monometallic Cu and bimetallic CuNi catalysts under illumination conditions undergo an oxidation process, fully reversible in the presence of reaction mixture. Contrary to the copper, XANES collected above the Ni K-edge demonstrated that Ni maintains a dominant Ni^{2+} both in surface and bulk positions, and only negligible changes were observed under illumination. By comparing the XANES measurements in the different depths of the catalytic bed for mono-Cu (left) and bimetallic CuNi (right) catalysts (Fig. 17B), the difference in Cu oxidation state between the two catalysts can be observed only for surface layer upon UV irradiation. The amount of each component was quantified from Cu *K*-XANES through linear combination fit. Thus, the authors demonstrated that 38 and 11 mol. % of copper appears in oxidized Cu^{2+} state in Cu and Cu–Ni samples, respectively, while the rest of copper remains as Cu^0. The observed difference between Cu and Cu–Ni catalysts would be significantly less obvious if the XAS experiment was performed using "standard" setups (lack of matching between X-ray and illumination photon volumes) which

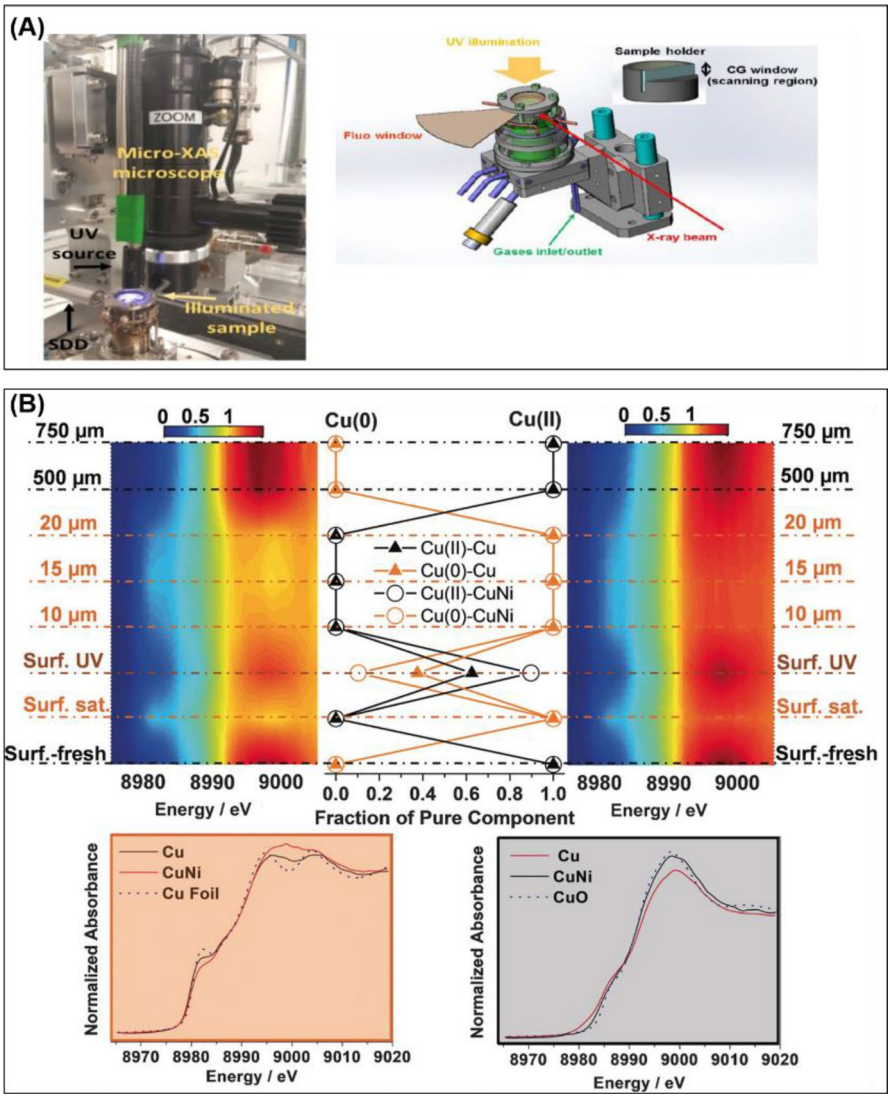

Fig. 17 **A** Photographic view of the experimental setup (left); schematic view of the measurement cell (right). Inset: sample holder. **B** Contour plot of Cu K-edge XANES spectra obtained under illumination for the Cu (left) and CuNi (right) samples. For the surface position, the two previous states (fresh sample and after gas saturation) are included. Concentration profiles (central part) and XANES spectra (bottom) corresponding to pure chemical species obtained from PCA are included. Colors in the central panel are assigned to pure species: Cu^{II} black, Cu^{0} orange. (Copyright with the authors permission [72])

will render a zerovalent metal XAS signal dominated by the exclusive effect of the reactants.

In the recent work reported by Piccolo et al. [73], a custom-made reactor cell was used for *operando* XAS experiment on photocatalytic hydrogen evolution over

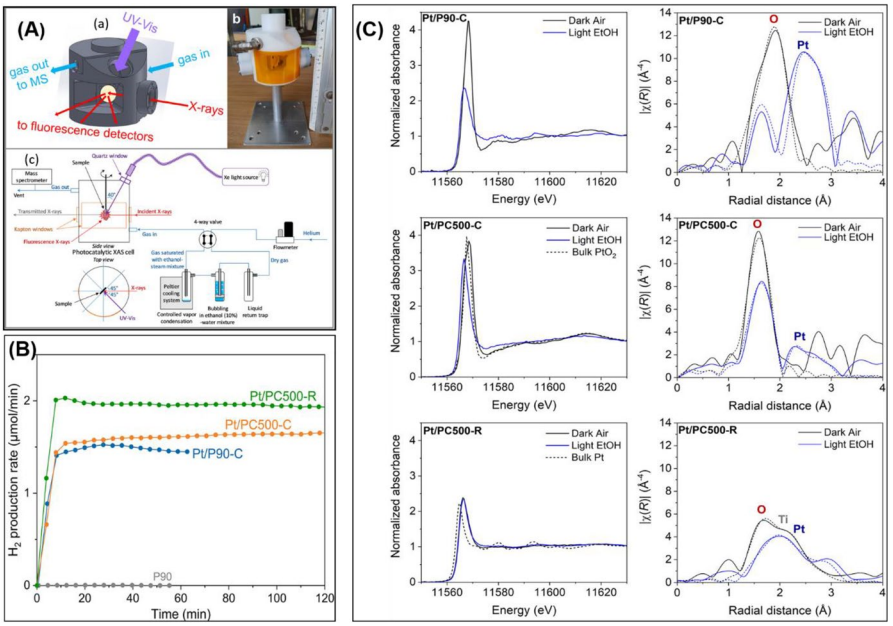

Fig. 18 **A** *Operando* XAS reactor setup: **a** scheme of the photocatalytic cell, **b** photograph of the cell, and **c** scheme illustrating the overall reaction setup. **B** Comparison of the various Pt (0.2 wt%)/TiO_2-based photocatalyst activities in the PHER from an ethanol/water/helium gas flow under UV irradiation at RT (laboratory reactor). **C** (left) Pt L_3-edge HERFD-XANES spectra of 0.2 wt% Pt/TiO_2 photocatalysts in the dark under atmospheric air (dark air) versus under UV–Vis irradiation in ethanol/water/helium gas flow (light EtOH). Bulk PtO_2 and Pt reference spectra are represented with dotted lines. (Right) Corresponding k^3-weighted EXAFS FT moduli. Best fits are represented with dotted lines. The radial distance is not phase-corrected. Rough positions of first-neighbor features are labeled with the proper elements. (Copyright with the authors permission [73])

Pt/TiO_2 catalyst. The cell, made from engineering thermoplastic (polyoxomethylene), was equipped with three Kapton windows for X-rays, thus allowing both transmission and fluorescence modes, and a quartz window for UV–Vis illumination (Fig. 18A). XAS data were recorded in partial fluorescence mode using a crystal spectrometer equipped with three spherically bent Ge (110) crystals in Rowland geometry and aligned at the maximum of the Pt-$L_{\alpha 1}$ line (9 442 eV). The sample in the form of self-supported pellet was located inside the cell, maintaining an angle of 45° between the accident beam and pellet surface and 90° between the incident beam and fluorescence cone. Illumination was delivered from the top part of the cell via an optical fiber connected to a Xe lamp (300 W). A four-way valve allowed flowing helium (100 mL/min) either directly to the cell or first passing through the saturator containing a mixture of ethanol (10%) and distilled water. *Operando* XAS experiments were performed in order to shed light on the observed difference in photocatalytic hydrogen evolution reaction (PHER) efficiency of the samples containing ultra-dispersed Pt species on TiO_2: P90-C, PC-500C, and PC-500R (where C and R stands for pre-calcined and pre-reduced, respectively). Among the tested

samples, the PC-500R exhibited the highest H_2 production rate (about 2 μmol/min), which is related to the presence of isolated Pt atoms coordinated solely by O and Ti from the support, known as strong metal–support interaction (Fig. 18B). By comparison with PtO_2 and Pt as references, it was shown that the formal oxidation state of Pt in pre-calcined samples is close to +4, while it is near zero for the pre-reduced sample (Fig. 18C). Under the photocatalytic conditions, the XANES of the pre-reduced sample remains almost unchanged, whereas the other two samples characterized by the white line (WL) peak decrease, and its shift to the lower energy (Fig. 18C). These observations clearly reveal the reduction of Pt species. An additional examination was performed through quantitative EXAFS analysis. Thereby, for the P90-C sample, EXAFS analysis revealed a switch from Pt–O to predominant Pt–Pt coordination, establishing Pt cluster formation under UV illumination. The PC500-C sample, which was initially supposed to contain mostly single Pt sites, demonstrated only slight clustering upon exposure to photocatalytic conditions. For the reduced Pt/PC500-R sample, in addition to Pt–O, the presence of Pt–Ti bonds were identified, which were not present for the other two samples.

3.3.2 *Operando* XAS for Investigating Photocatalysis in Liquid Phase

In the recent work by Spanu et al. [74], *operando* XAS was performed in fluorescence mode to study the PHER reaction over NiCu-TiO_2 catalyst under UV light irradiation in water–methanol solution. The cell adopted for XAS measurements was equipped with a Mylar window to ensure transparency both for X-rays and UV light (Fig. 19A). Both the UV LED source and the passivated implanted planar silicon (PIPS) fluorescence detector were located on the same side from the incident X-ray beam. The authors declared that the reported cell design maximizes X-ray fluorescence signals by adopting the possibility to work with minimized thickness of solution layer in front of the sample. The experiment was performed at the P65 beamline (DESY-Petra III). From the dark-conditions XANES analysis, it was concluded that (1) NiCu nanoparticles undergo surface oxidation when exposed to air, (2) partial dissolution of surface Cu oxides occurs in ethanol–water, and (3) less dissolution of Ni oxides occurs due to the less exposed Ni phase left behind by TiO_2 NTs and protected by Cu. Under illumination, Cu and Ni, entirely in metallic form (~ 100%, Fig. 19Bc, d), are active and can promote H_2 evolution via a Schottky junction-type mechanism. The authors emphasize that their findings differ significantly from those reported earlier by Muñoz-Batista et al. [72] on the similar catalytic system but in gas phase conditions, where dissolution and redeposition of Cu and Ni is not possible.

Photoelectric water oxidation using XAS has been recently reviewed by Deng et al. [61]. Here, we will give one example on the effect of illumination and potential on the oxidation state of FeNi overlayers on hematite photoanodes during water photo-oxidation [92]. Fe and Ni K-edges fluorescent XAS has been employed to track possible changes in an FeNi overlayer under different conditions. The FeNi hydroxide layer with 30-nm thickness (Fig. 20A) covered with 1 M of NaOH aqueous electrolyte was deposited in a special electrochemical cell previously employed for *operando* XAS on a WO_3 photoanode [93]. A high-power white light-emitting

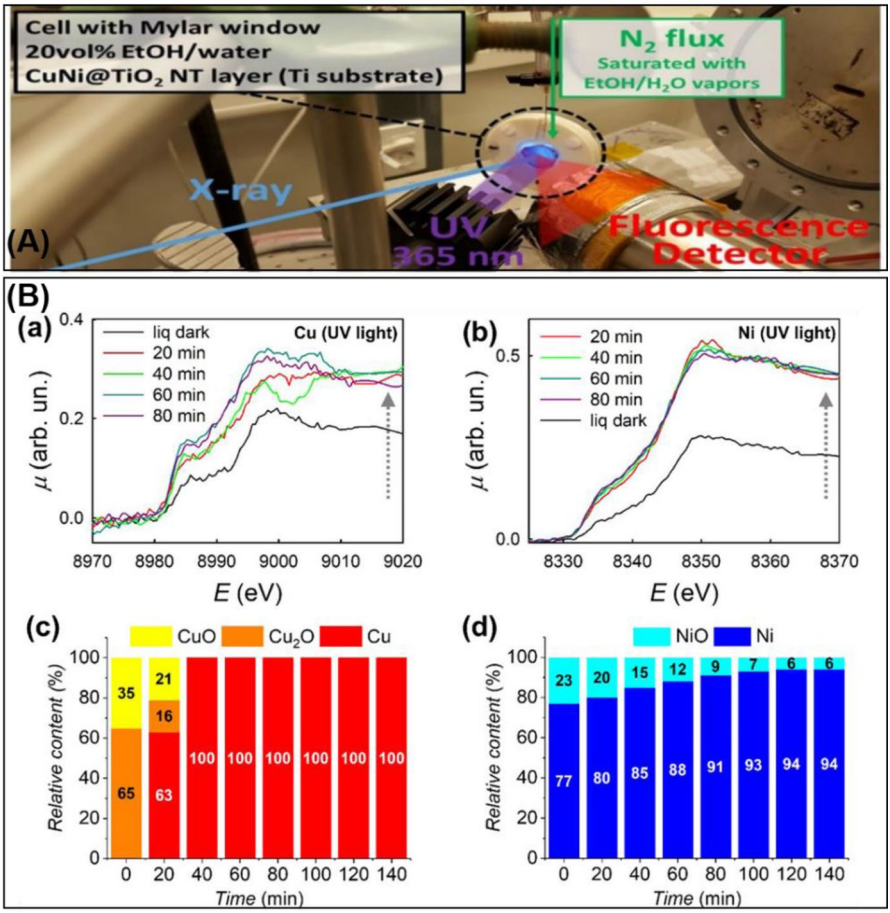

Fig. 19 **A** Cell and sample environment from XAS *operando* liquid-phase experiment on photocatalytic H_2 evolution over NiCu-TiO_2 catalyst. **B** XAS spectra of **a** Cu K-edge and **b** Ni K-edge XAS spectra of 5Ni5Cu–TiO_2 immersed in the cell in a water–ethanol solution under UV light illumination for different exposure times; the last recorded XAS spectra for 5Ni5Cu immersed in the water−ethanol solution under dark conditions are reported as reference, which defines the sample condition prior to UV illumination; see black curves. **c** Cu and **d** Ni phase compositions determined by *operando* XAS measurements for $5Ni_5Cu$–TiO_2 immersed in a degassed ethanol–water solution under UV light irradiation. (Copyright with the authors permission [74])

diode (ca. 100 mW/cm^2) was used in the photocatalytic test. The experiment was performed at the P64 beamline of the PETRA III synchrotron. It was shown that the change of Fe K-edge XANES signal with potential was very small, but it became more pronounced under illumination. In contrast, Ni sites were more strongly affected by both potential and illumination (Fig. 20B). Combining the findings from both "dark" and "light" experiments, it was revealed that both electrons and holes can be transferred between the hematite layers and FeNi overlayer. On the basis of linear combination fit of the XANES data set collected at both conditions (using

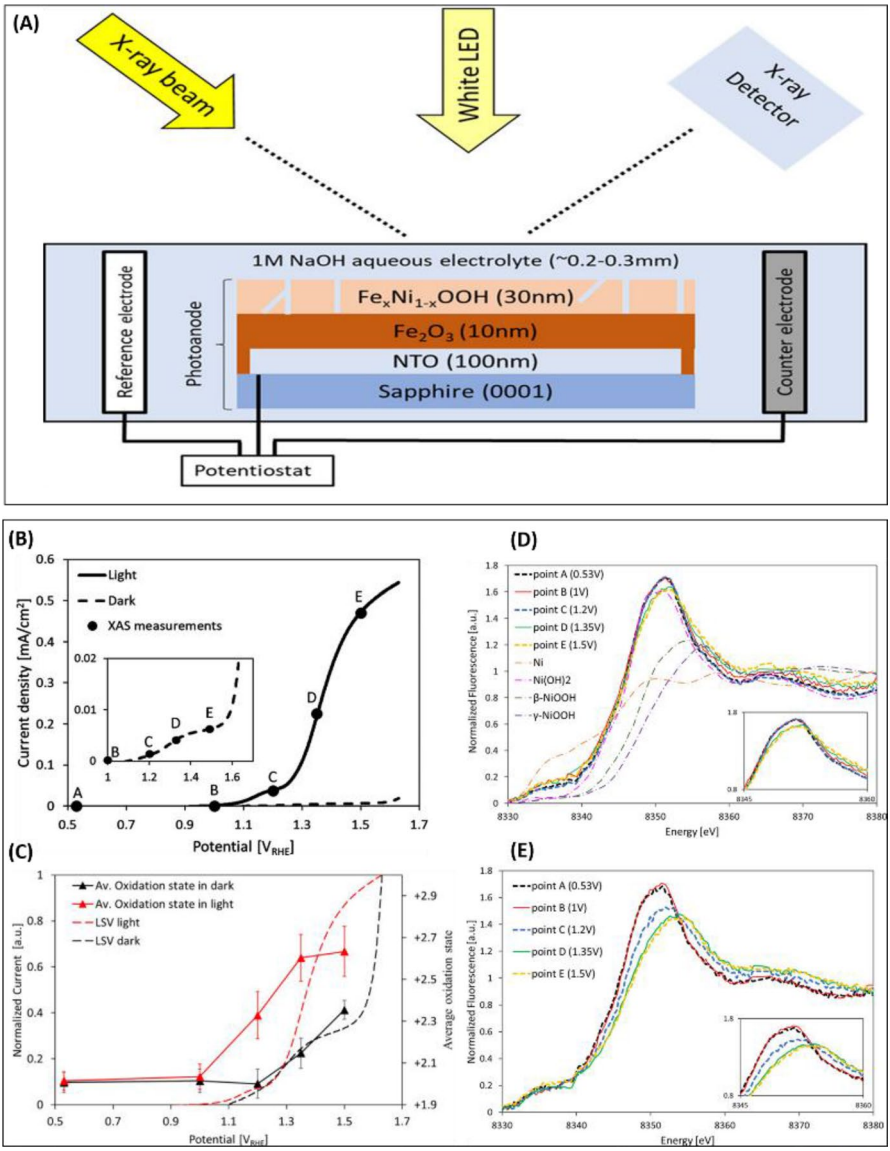

Fig. 20 **A** Schematic top-view illustration of the *operando* XAS experiment. **B** LSV voltammograms measured under dark (dashed line) and light (solid line) conditions within the beamline before the XAS measurements for hematite/FeNi (oxy)hydroxide. **C** Average oxidation state of Ni under dark (solid line with black triangles) and light (solid line with red triangles) conditions for hematite/FeNi, overlaid on the LSV voltammograms recorded during the XAS measurement under the same conditions. Dark and light currents were normalized by dividing by their respective currents at 1.63 V_{RHE}. **D**, **E** Normalized Ni K-edge XANES spectra for hematite/FeNi (oxy)hydroxide under **D** dark and **E** light conditions. All of the potentials are versus RHE. Normalized Ni K-edge XANES spectra for NiO, β-NiOOH, and Ni standards used for the fitting are also presented in panel **e**. (Copyright with the authors permission [92])

NiO, β-NiOOH, and for γ-NiOOH as a reference for +2, +3 and +3.6 oxidation states, respectively), the authors quantified the averaged Ni charge state under different voltages. Overall, the authors demonstrated that Ni sites need to be oxidized for more efficient oxygen evolution reaction (OER). It was shown that the illuminated conditions allow Ni oxidation at the lower potentials due to the generated additional photovoltage. The quantitative analysis demonstrated the Ni oxidation state saturated at ca. 2.6 ± 0.1 under illumination conditions.

4 Time-Resolved Techniques in Photocatalysis

Time-resolved techniques are frequently used to track a quick process in a given reaction at a high time resolution (sub-millisecond to nanoseconds). These measurements can provide valuable information in photocatalytic reaction to elucidate the microscopic mechanisms of photogenerated charge generation, transfer/recombination of charge carriers, and surface reaction kinetics. Since numerous spatial and/or temporal resolution techniques have emerged over the years and reviewed recently in details [94–103], in this part, we will briefly discuss the time-resolved FTIR, the transient absorption, and photoluminescence spectroscopies by giving one to two examples for each technique used in photocatalysis.

4.1 Time-Resolved FTIR

The charge transfer can be studied from ms (rapid scan) to ns (step scan) by time-resolved FTIR depending on duration of the event (Scheme 4A). In the rapid scan (Scheme 4B), the interferometer mirror moves very fast, and each full forward–backward interferometer scan allows extraction of up to four spectra. However, the number of spectra per second depends on spectral resolution since the duration of one scan is related to both mirror distance and velocity. For example, VERTEX 80/80v, from Brucker, can achieve around 110 spectra per second with 16 cm^{-1} of resolution. Step-scan (Scheme 4C) technique is often used to monitor the temporal progress of very fast events (transients). The interferometer mirrors are set at a precise position where interferogram points are collected. Then, the moving the mirror are translated to a next position and the experiment is restarted again. Therefore, a highly reproducible experiment is required in the step-scan mode. The time resolution corresponds to the response of the detector and can reach a few nanoseconds.

In a recent study, an ultrafast time-resolved quantum cascade laser (QCL)-assisted *operando* FTIR was used to monitor the photo-oxidation of MeOH over TiO_2 P25, commercial anatase (TiO_2 CA), and homemade anatase (TiO_2 HA) at a resolution time of few μs [5]. The new setup operates in rapid-scan mode with four quantum cascade lasers emitting at different wavenumbers. Each sample was subject to several photocatalytic tests with three successive UV on/off cycles under 0.1 vol.% of methanol and 20 vol.% of oxygen with a 30-cc.min^{-1} flow rate at 25 °C. At each wavenumber, the QCL (pulse rate = 10,000 Hz, time resolution = 100 μs) was tuned to monitor the formation (lamp on) and conversion (lamp off) of formate species

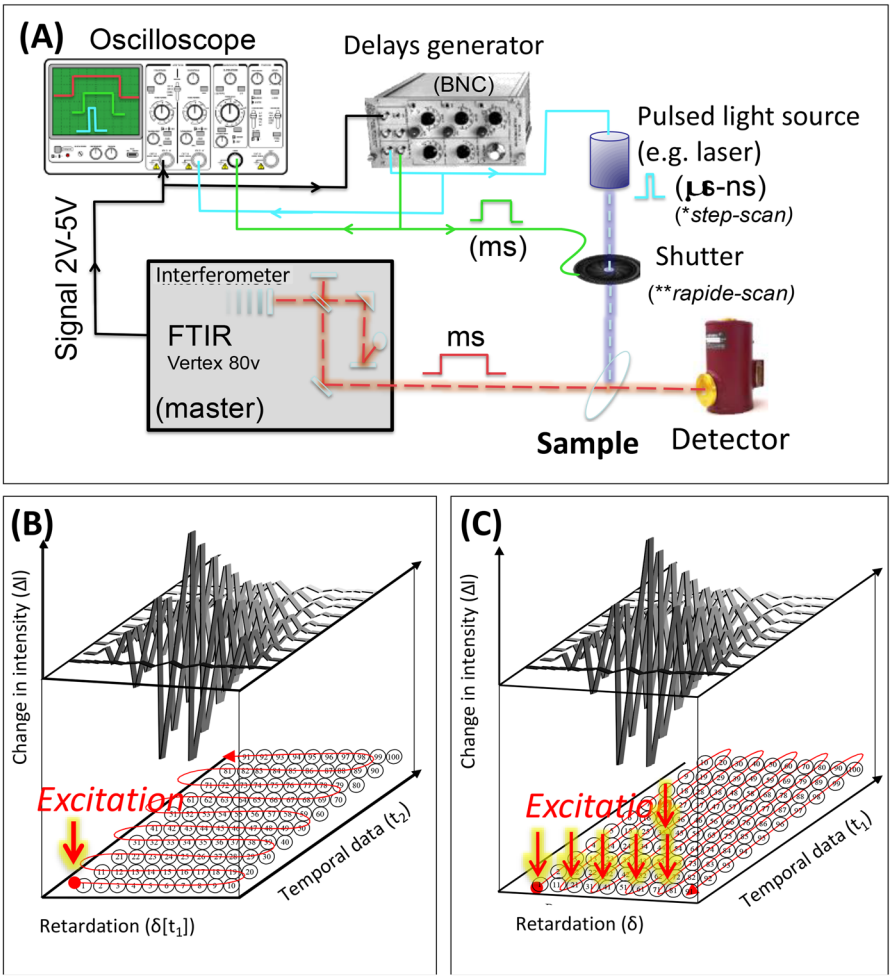

Scheme 4 **A** Scheme of the time-resolved FTIR setup in **B** rapid-scan and **C** step-scan modes

at 1360, 1380, 1564, or 1580 cm^{-1}. A direct relationship between the decomposition of surface formate species and the MeOH conversion rate (total yield of methyl formate + CO_2) was established: the faster the reaction of surface formate species, the higher the photo-oxidation activity. This was confirmed by the evolution of the QCL beam absorbance at 1360 cm^{-1} over TiO_2 P25, TiO_2 CA, and TiO_2 HA during the first UV on/off cycle and the corresponding apparent rate of formate formation (lamp on, Fig. 21Aa–c) and reaction (lamp off) (Fig. 21Ad–f). Once the UV lamp is turned on, the accumulation of formate species on the catalyst surface was observed at different rates depending on the photocatalyst until reaching the steady state, while these species decreased when the lamp is turned off due to their further conversion. The apparent rate of both formate formation and reaction are higher for TiO_2 P25 than the other two samples, which is directly correlated to its superior

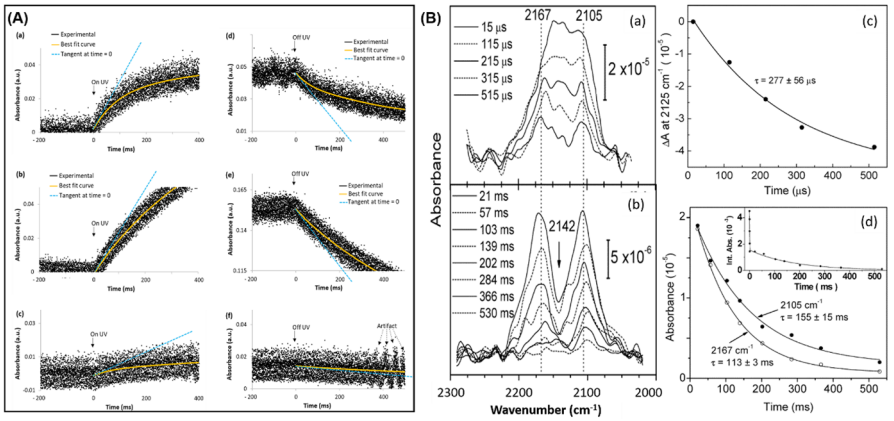

Fig. 21 **A** QCL beam absorbance at 1360 cm^{-1} vs. time over TiO_2 P25 (a and d), TiO_2 CA (**b** and e), and TiO_2 HA (c and f) during the first UV on/off cycle (UV on a–c, UV off d–f) under reaction flow at 25 °C and atmospheric pressure; flow conditions = 30 mL/min; 0.1 and 20 vol.% of methanol and oxygen in argon, respectively; Hg–Xe lamp (200 W); irradiance = 200 mW/cm^2; In (a–c); time = 0 corresponds to the moment when the shutter between the lamp and the UV light guide attached to the IR cell was opened to irradiate the sample. During the preceding 200 ms, the sample was already under reaction flow but still in the dark; In (d–f); time = 0 corresponds to the moment when the shutter was closed again still under reaction flow. The fall times to open and to close the shutter were around 6.5 ms and 3.2 ms, respectively, with a minimum pulse width of 13 ms. **B** Time-resolved FTIR absorption spectra of CO formed inside MCM-41 recorded upon laser-induced photolysis of DPCP: (a) step-scan FTIR spectra (average of 21 experiments) and (b) rapid-scan FTIR spectra (average of 12 experiments). The rapid-scan spectra were normalized so that (a) and (b) correspond to the same amount of DPCP depleted (and CO produced) per laser pulse. Note that the absorbance scale of the millisecond spectra is enlarged. (c) Single-exponential fit of the absorbance difference at 2125 cm^{-1} yields a decay time of 277 ± 56 µs. Corrected for the 1420-µs RC high-pass filter of the detector yields 344 ± 70 µs. (d) Single-exponential fit of the absorbance decay at 2105 and 2167 cm^{-1} yields decay times of 155 ± 15 ms and 113 ± 3 ms, respectively. The inset shows the decay of the full CO profile (integrated from 2220 to 2060 cm^{-1}) in both the rapid-scan data and the step-scan data (corrected for the RC high-pass filter of the detector). Ordinate unit of inset = 10^{-3} cm^{-1}. (Copyright with permission from Refs. [5, 107])

photocatalytic activity. The conversion of formate was found to be the rate-limiting step. Other studies conducted by Frei et al. to monitor photocatalytic reactions using the rapid-scan method can be consulted elsewhere [104–106].

In the nanoseconds regime, only few transient step-scan FTIR studies on photocatalytic systems have been published so far [95, 107]. For example, Frei et al. studied the dynamics of CO in the channels of MCM-41 during the photodissociation of diphenyl cyclopropenone (DPCP) at RT by time-resolved FTIR using both the step-scan and rapid-scan methods [107]. The time-resolved measurements were conducted with a Bruker Model IFS88 spectrometer and initiated by 355-nm pulses of a Quanta Ray model. In the step-scan experiments, the IR spectra were recorded from 0 to 530 µs with a time resolution of 1 µs. In the rapid-scan experiments, the mirror velocity was 160 kHZ with a spectral resolution of 8 cm^{-1}. The study revealed the biphasic kinetics of CO diffusion in MCM-41 during the DPCP photolysis: the fast escape, in µs, of the physiosorbed/or weakly adsorbed CO molecules and the slow residence, in ms, of CO molecules trapped between silanol

groups, diphenyl-acetylene co-product, and probably DPCP. From the time-resolved FTIR data in the region of the CO band (2220–2060 cm^{-1}), the initial band centered at 2130 cm^{-1} decays in the μs timescale and emerged into two peaks at 2167 and 2105 cm^{-1} (Fig. 21Ba). The last two bands decay much more slowly after hundreds of ms (Fig. 21Bb). The different decay times indicate the biphasic release of CO from the mesopores as confirmed by the time evolution of the integrated CO absorption spectrum (2220–2060 cm^{-1}) Fig. 21Bc–d).

4.2 Time-Resolved Microwave Conductivity (TRMC)

TRMC is a useful technique for studying the primary processes in photocatalysis, i.e., the charge carrier dynamics with nanosecond time resolution [108]. During TRMC measurements, the semiconductor is illuminated by a nanosecond laser pulse which induces a change in the microwave power reflected from the sample. The microwave power can be then correlated to the photoinduced change in the sample conductance from which information on the charge carrier generation, charge carrier trapping, charge carrier recombination, and electron/hole transfer can be obtained. Very recently, the TRMC technique was used to investigate the facet-dependent carrier dynamics of Cu_2O governing the photocatalytic H_2 production from water under

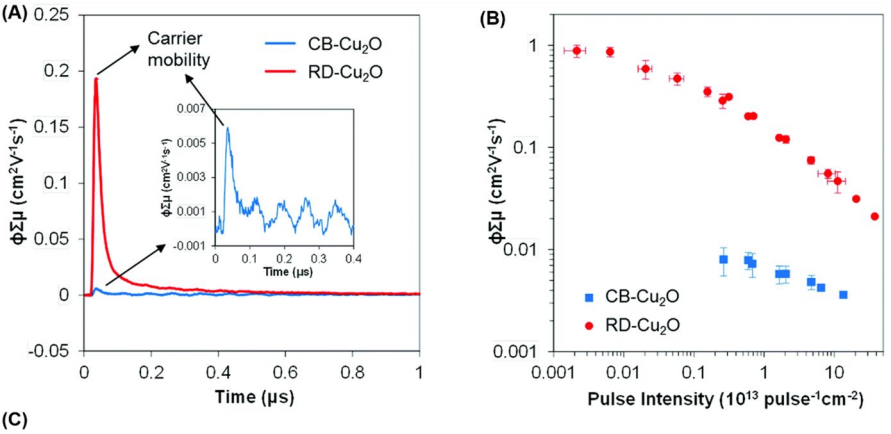

(C)

Samples	Carrier lifetime, τ_{eff} (ns) τ_1	τ_2	Diffusion length, $L_{D,eff}$ (nm) From τ_1	From τ_2	Δσ (S/cm)	N_a (cm^{-3})
CB-Cu_2O	14.3 ± 1.5	257.0 ± 8.8	14.7 ± 0.7	63.2 ± 11.4	1.07	1.20×10^{21}
RD-Cu_2O	22.2 ± 4.0	281.0 ± 9.1	97.9 ± 10.3	280.9 ± 38.	0.37	1.19×10^{19}

Fig. 22 **A** TRMC signal of CB-Cu_2O and RD-Cu_2O over time at 7.0×10^{12} photon $pulses^{-1}$ cm^{-2}, with the inset showing the magnification of the signal of CB-Cu_2O, and **B** maximum TRMC signal as a function of incident pulse intensity of CB-Cu_2O and RD-Cu_2O. **C** Summary of average effective charge lifetime, diffusion length, and parameters involved in dark microwave conductivity measurement of CB-Cu_2O and RD-Cu_2O. (Copyright with permission from Ref. [109])

visible light [109]. The results show that the photoactivity of rhombic dodecahedral Cu_2O with dominant {110} facets (RD-Cu_2O) was 1.5-fold higher than that of cubic Cu_2O with {100} surfaces (CB-Cu_2O). This is was explained by the higher carrier mobility of RD-Cu_2O compared to CB-Cu_2O at different laser pulse intensities, as revealed from TRMC measurements (Fig. 22A, B). Both carrier lifetimes (τ_1 and τ_2) and diffusion lengths (Fig. 21C), determined from the decay of the TRMC signals, are smaller for CB-Cu_2O than that of RD-Cu_2O, suggesting that the charge carriers recombine/trap faster in CB-Cu_2O due to the presence of more structural defects in this sample. The higher conductivity (σ) and higher carrier density (N_a) of CB-Cu_2O, determined by dark microwave conductivity measurements (Fig. 22C), confirm the presence of more defects in CB-Cu_2O than RD-Cu_2O, which contribute to electron trapping and result in low photocatalytic activity.

4.3 Photoluminescence (PL) Spectroscopy

PL spectroscopy is a light emission process from the electronic excited state of a molecule or materials to its ground state after excitation by an external light source. In photocatalysis, PL spectroscopy is widely used as one of the fundamental characterization tools to study the excited-state properties from ns to ms at a molecular level with high sensitivity and nondestructive nature. Time-resolved PL spectroscopy was used to explore the excited-state properties of the novel bimetallic supramolecular assembly of pyrene-modified photosensitizer and RuPy···ReCOPy used for CO_2 photoreduction under visible light [34]. It was shown that the novel assembly showed higher photocatalytic activity than the benchmark system [$Ru(bpy)_3Cl_2$(Ru) with $Re(bpy)(CO)_3Cl$ (ReCO)]. This is due to an efficient electron transfer from the Ru center to the pyrene moiety in RuPy and from the latter to the rhenium center in ReCOPy. This is confirmed by the red-shifted PL (620 vs. 670 nm) and the higher excited-state lifetime (0.13 vs. 0.9 µs) of ^{3}RuPy compared to ^{3}Py, allowing a stronger Ru-Py interaction and a better electron transfer to rhenium (Fig. 23Aa–b. Furthermore, the ^{3}RuPy exhibits less sensitivity to the oxygen (inset in Fig. 23Aa–b) and a faster electron transfer than ^{3}Py, concluded from the quenching of the ^{3}MLCT with triethanolamine (TEOA).

4.4 Transient Absorption (TA) Spectroscopy

Transient absorption (TA) spectroscopy is used to evaluate the lifetimes of photogenerated charge carriers in a range of ps to ns. If we come back to a previously discussed example[34], the red-shifted PL of ^{3}RuPy compared to ^{3}Py was also observed in the transient absorption of this complex, in addition to a new absorption transient at 520 nm with longer lifetime of 35 µs, probably assigned to the (^{3}(RuPy···RuPy) exciplex (Fig. 23Ac–d). By using TA spectroscopy, it was shown that the presence of defects (O_v) in a WO_3 structure can generate more electron-trapping states which inhibit the recombination of electron–hole pairs and increase the photocatalytic oxygen evolution [110]. This effect can be enhanced in presence of Pt as cocatalyst in a O_v-WO_3 structure. In WO_3 (Fig. 23Ba), two decays were observed

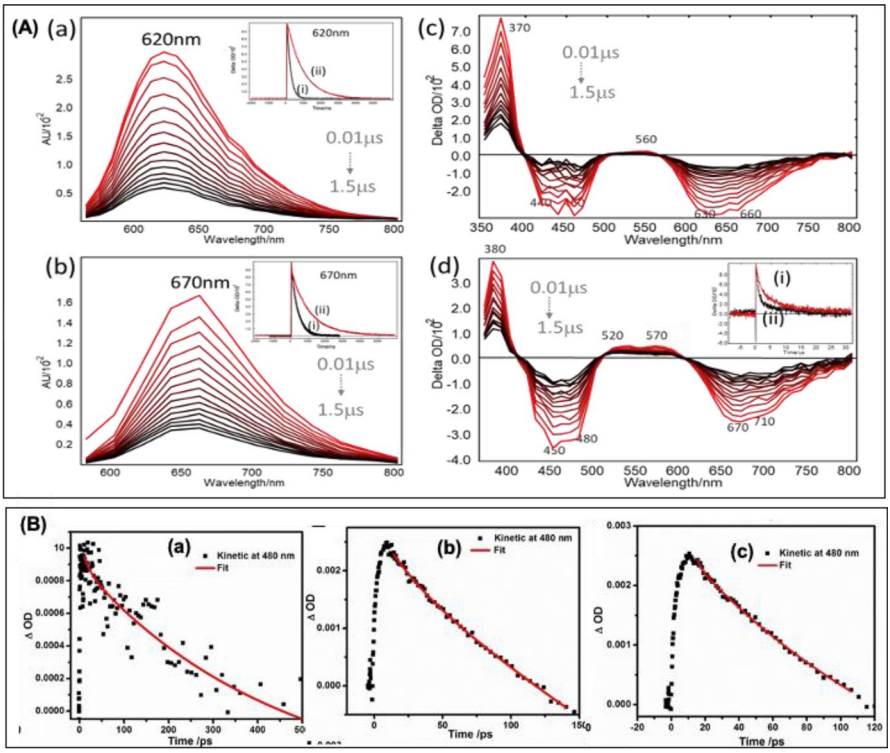

Fig. 23 **A a**, **b** correspond to the nanosecond emission spectra (140 ns/spectrum) of the ^{3}MLCT of Ru and RuPy, respectively. Inset = normalized kinetic decay trace of ^{3}MLCT emission of Ru and RuPy monitored at 620 nm and 670 nm, respectively, under air (i) and argon (ii) atmospheres. **c**, **d** Report of the evolution vs. the time (140 ns/spectrum) of the absorption transition (AT) of Ru and RuPy. Inset of Fig. d = normalized kinetic decay traces of the AT at 520 nm (i) and 570 nm (ii). λ_{exc} = 532 nm; [RuPy] = 1.7 mM; [Ru] = 3 mM; all spectra were recorded under Ar at 298 K. (B) The kinetics of decay monitored at 480 nm of **A** WO_3, **B** O_v-WO_3-600, and **C** O_v-WO_3-Pt. (Copyright with permission from Refs. [34, 110])

at 15.3 and 541.7 ps, characteristics of the fast charge recombination and electron trapping, respectively. In contrast, significantly longer lifetimes of the excited states (τ_1 = 27.1 ps and τ_2 = 749.1 ps) were obtained for O_v-WO_3 due to the electron-trapping states (Fig. 23Bb). The heterojunction between the noble Pt and O_v-WO_3 effectively reduces the recombination of charge carries with ultrafast electron injection from trap states to the metal (Fig. 23Bc).

5 Summary, Limitations, and Outlook

In this review, we summarized the recent efforts of using in situ and *operando* techniques, e.g., FTIR, Raman, EPR, XAS, and time-resolved spectroscopy, to perform real-time observations of one of the most complicated and multifunctional process, photocatalysis.

In situ IR spectroscopy can provide valuable and pertinent information on the adsorption sites of photocatalyst, both directly or via the adsorption of probe molecules (the reactants themselves are always the best probe molecules). Physical chemical properties such as acidity, basicity, and redox properties of the photocatalysts can be also described and quantified in strength and as site concentrations. In situ FTIR can be also be utilized for real-time analysis of the gas products in photocatalysis, which allows determining the reaction selectivity and photocatalyst performance, but cannot provide information on the evolution of catalyst surface during the reaction. IR *operando* technique can complete simultaneous monitoring of surface and gas/or liquid species as the best way to establish the reaction pathways. It is possible to observe at what time different intermediates or by-products are formed and to deduce which site (active site or spectator) is responsible for a given photocatalytic step. In such a way, it is possible, step by step as a jigsaw puzzle, to reconstruct the whole reaction mechanism. However, studying very short-lived intermediates cannot be achieved with standard FTIR spectroscopy. Thus, very high time resolution (μ to ns) is mandatory and can be achieved by using special recording techniques such as step-scan and rapid-scan interferometry. In this case, photocatalytic experiment needs to be well controlled in time but also highly reproducible.

Raman spectroscopy is used to monitor the structural transformation of photocatalysts and to identify the reaction intermediates under real reaction conditions. However, the application of *operando* Raman spectroscopy in photocatalytic reaction is still limited because of the overwhelming of photocatalysis excitation light with Raman photons and the low signal intensity resulting from the low frequency of the Raman scattering effect. The latter drawback has been overcome by development of new experimental techniques [e.g., surface-enhanced Raman spectroscopy (SERS), shell-isolated nanoparticle-enhanced Raman spectroscopy (SHINERS), or tip-enhanced Raman spectroscopy (TERS)]; however, application of those approaches imposes limitations on systems and reactions to characterize, particularly if *operando* conditions in photocatalysis are sought.

EPR spectroscopy has been widely used in photocatalysis for monitoring the charge carrier trapping, recombination and transfer, identification of reactive radicals/oxygen species, and direct observation of the paramagnetic active species in photocatalysis. However, the EPR measurements are often performed in the presence of a spin trap and/or at low temperature (below 77 K) in order to improve detection of the highly reactive species with unpaired electrons. Due to these specific drawbacks, the application of EPR in photocatalysis is still scarce under *operando* conditions.

X-ray absorption spectroscopy represents a powerful technique to investigate structural and electronic configuration of metal sites in nanostructured and bulk

catalysts. XANES allows us to probe variation in oxidation state, density of unoccupied stats, and chemical bond hybridization, while EXAFS is more sensitive to bond lengths and coordination environment. Compared to the other techniques (IR, Raman), XAS presents the advantage in both surface and bulk sensitivities. However, *operando* XAS experiments in photocatalysis are mainly conducted at synchrotron facilities, which limits the available experimental setup and the possibility of performing long-term experiments. Therefore, the development of additional suitable laboratory-based XAS setups with the implementation of adequate *operando* cells is necessary for performing long-term experiments in house and extending the characterization timescales.

Time-resolved techniques, such as time-resolved FTIR, time-resolved microwave conductivity (TRMC), transient absorption spectroscopy, and photoluminescence spectroscopy, are frequently used to track the quick process in photocatalysis in submillisecond to picoseconds timescales. These measurements can be used to study the photogenerated charge generation, transfer/recombination of charge carriers, and their lifetimes. Some works have already given important insights in this field, but many of these methods need to be adapted to investigate the photocatalysts under reaction conditions.

However, a more comprehensive picture of a working photocatalyst is still necessary for the quest of the entire mechanistic process in order to extract design principles for more active and/or stable photocatalysts. Therefore, improved experimental studies with combined techniques such as IR, Raman, XAS, and EPR can provide a detailed picture of photocatalytic systems. Furthermore, other techniques not mentioned above such as nuclear magnetic resonance (NMR), UV–Vis, XPS, neutron spectroscopy, and microscopies, operated in situ or using *operando* methodology, can provide complementary information about photocatalytic systems. Thus, a range of powerful methods must be used together in order to probe the photocatalytic processes in a spatiotemporal manner with the time domain from femtoseconds to milliseconds and the space domain from 0.1 nm to 10 mm.

6 Concluding Remarks

Understanding the structure–activity/selectivity relationship is of a significant importance to design new materials with high performance in photocatalysis. In situ spectroscopic techniques have been widely used to provide fundamental information about the photocatalyst structure and surface species under controlled conditions, i.e., under vacuum, in the presence of a probe molecule or a under reactive atmosphere (O_2, H_2, etc.). For example, the in situ FTIR technique can be used as a characterization tool for the (1) determination of oxidation/coordination state of the active sites, (2) identification/quantification of Lewis and Brønsted acidity, and (3) calculation of the entropy and enthalpy of adsorption. However, this technique is essentially limited to the characterization of surface species, thus it is important to be used in complement with other techniques such as in situ Raman and XAS. On one hand, in situ Raman spectroscopy is used to investigate the surface properties of photocatalysts, i.e., to analyze the structure of photocatalysts and their changes

under controlled conditions. On the other hand, in situ EPR provides information on the radical and unpaired electron species formation, while XAS is related to the structural/electronic configuration of metal sites of the photocatalysts. In situ measurements can also be conducted under reaction conditions to identify the reaction intermediates and reveal the reaction mechanism in photocatalysis. However, it is an indirect method, since the reaction is performed under special conditions (partial vacuum) and the surface and gas/liquid phase analysis are performed separately. Thus, true understanding of the structure–activity/selectivity relationship requires the monitoring of photocatalysts under realistic catalytic conditions which points to the importance of *operando* spectroscopy (e.g., *operando* FTIR, *operando* Raman, *operando* XAS, etc.). This methodology allows simultaneous monitoring of the catalyst surface and the gas/liquid phase on the same sample under real reaction conditions. Note that the design of the associated reaction cell and the reaction conditions are critical here and can affect the overall performance of the photocatalytic process. However, some intermediates remain elusive under steady-state conditions of *operando* spectroscopy. Thus, the use of transient conditions (for example, via isotopic substitution, i.e., using the SSITKA approach) is sometimes of particular significance. Time resolution and discrimination of reaction intermediates can also be done by modulation excitation spectroscopy, allowing discrimination of transient states. Time-resolved (TR) techniques are also required to detect and determine the reactivity and kinetic significance of reaction intermediates that would otherwise escape detection at steady state. For example, TR FTIR techniques allow monitoring the photocatalyst surface at the timescale of 10 ms and slower by using the rapid-scan method. For FTIR monitoring in the time range from 10 ns to μs, the step scan is the method of choice. Time-resolved microwave conductivity (TRMC) is a useful technique to study charge carrier generation, trapping, and recombination, as ultrafast processes that occur at very short times (femto–nano seconds) after irradiation of photocatalysts. Moreover, PL and TA spectroscopy can be used to study the excited-state properties from ns to ms at a molecular level and to follow the short lifetimes of photogenerated charge carriers in range of ps to ns, respectively. However, catalysis occurs in time and space [111], thus *operando* imaging during reaction is the next big step to understand catalysis in shaped catalysts, which will be particularly challenging when it comes to photocatalytic processes.

Since the overall efficiency of photocatalysis is the multiplication of all the elemental efficiencies, the latter should be measured together for a reaction. However, in the presented case study, only one or two techniques were used to monitor the photocatalytic reaction under reaction conditions which cannot allow identification of all the elemental steps and increases the incoherent reproducibility caused by separated measurements. Thus, the use of multiple techniques and/or a multidisciplinary approach in one photocatalytic reaction to conduct measurements and modeling of all these steps is required to fully understand and improve the efficiency of photocatalysis. For example, the combination of *operando* XAS and FTIR can provide deep insight into the understanding of the dynamic structure of photocatalysts and the formation of surface intermediates under the reaction conditions. On the other hand, the development of in situ*/operando* techniques to monitor photocatalytic reactions at pilot scale or even industrial scale under real industrial conditions

is also envisaged, so that future researches will be more efficient and less time- and money-consuming.

Acknowledgements Mohamad El-Roz and Houeida Issa Hamoud acknowledge the Normandy Region (H_2CO_2 Project) for the financial support. Lukasz Wolski gratefully acknowledges the Foundation for Polish Science (FNP) (decision no. START 95.2021) and the Polish Minister of Education and Science (decision no. SMN/16/0997/2020) for the financial support. Ilia Pankin acknowledges the Ministry of Science and Higher Education of the Russian Federation for financial support (State assignment in the field of scientific activity, № 0852-2020-0019).

Author Contributions The manuscript was prepared and written through the contributions of all authors. All authors have approved the final version of the manuscript.

Declarations

Conflict of interest On behalf of all authors, the corresponding author states that there is no conflict of interest.

References

1. Turro NJ, Ramamurthy V, Scaiano JC (2017) Modern molecular photochemistry of organic molecules. Viva Books, University Science Books, Sausalito. https://doi.org/10.1002/anie.201003826
2. Takanabe K (2017) Photocatalytic water splitting: quantitative approaches toward photocatalyst by design. ACS Catal 7(11):8006–8022. https://doi.org/10.1021/acscatal.7b02662
3. Coy E, Siuzdak K, Grądzka-Kurzaj I, Sayegh S, Weber M, Ziółek M, Iatsunskyi I (2021) Exploring the effect of BN and BN bridges on the photocatalytic performance of semiconductor heterojunctions: enhancing carrier transfer mechanism. Appl Mater Today 24:101095. https://doi.org/10.1016/j.apmt.2021.101095
4. El-Roz M, Bazin P, Daturi M, Thibault-Starzyk F (2013) Operando infrared (IR) coupled to steady-state isotopic transient kinetic analysis (SSITKA) for photocatalysis: reactivity and mechanistic studies. ACS Catal 3(12):2790–2798. https://doi.org/10.1021/cs4006088
5. Schnee J, Daturi M, El-Roz M (2020) Ultrafast time-resolved quantum cascade laser diagnostic for revealing the role of surface formate species in the photocatalytic oxidation of methanol. Catal Sci Technol 10(16):5618–5627. https://doi.org/10.1039/D0CY00865F
6. Kim DW, Leem YA, Yoo SD, Woo DH, Lee DH, Woo JC (1993) Measurement of the exciton binding energy in a narrow GaAs–AlxGa1−xAs quantum well by photoluminescence excitation spectroscopy. Phys Rev B 47(4):2042. https://doi.org/10.1103/PhysRevB.47.2042
7. Inoue Y (2009) Photocatalytic water splitting by RuO_2-loaded metal oxides and nitrides with d 0-and d 10-related electronic configurations. Energy Environ Sci 2(4):364–386. https://doi.org/10.1039/B816677N
8. Weckhuysen BM (2002) Snapshots of a working catalyst: possibilities and limitations of in situ spectroscopy in the field of heterogeneous catalysis. Chem Commun 2:97–110. https://doi.org/10.1039/B107686H
9. Weckhuysen BM (2015) Studying birth, life and death of catalytic solids with operando spectroscopy. Natl Sci Rev 2(2):147–149. https://doi.org/10.1093/nsr/nwv020
10. Jones CW, Tao F, Garland MV (2012) Introduction to special issue on operando and in situ studies of catalysis. ACS Catal. https://doi.org/10.1021/cs3006692
11. Bañares MA (2005) Operando methodology: combination of in situ spectroscopy and simultaneous activity measurements under catalytic reaction conditions. Catal Today 100(1–2):71–77. https://doi.org/10.1016/j.cattod.2004.12.017
12. Ferri D (2021) Toward operando infrared spectroscopy of heterogeneous catalysts. Heterog Catal Adv Des Char Appl 1:311–338. https://doi.org/10.1002/9783527813599.ch18
13. Rasmussen SB, Perez-Ferreras S, Bañares MA, Bazin P, Daturi M (2013) Does pelletizing catalysts influence the efficiency number of activity measurements? Spectrochemical engineering

considerations for an accurate operando study. ACS Catal 3(1):86–94. https://doi.org/10.1021/cs300687v
14. Harrick NJ (1979) Internal reflection spectroscopy. Harrick Scientific Corporation, New York
15. Vimont A, Thibault-Starzyk F, Daturi M (2010) Analyzing and understanding the active site by IR spectroscopy. Chem Soc Rev 39(12):4928–4950. https://doi.org/10.1039/B919543M
16. Lercher JA, Grundling C, Eder-Mirth G (1996) Infrared studies of the surface acidity of oxides and zeolites using adsorbed probe molecules. Catal Today 27(3):353–376. https://doi.org/10.1016/0920-5861(95)00248-0
17. Hadjiivanov KI, Vayssilov GN (2002) Characterization of oxide surfaces and zeolites by carbon monoxide as an IR probe molecule. Elsevier, New York. https://doi.org/10.1016/S0360-0564(02)47008-3
18. Ivanova E, Mihaylov M, Aleksandrov HA, Daturi M, Thibault-Starzyk F, Vayssilov GN, Hadjiivanov KI (2007) Unusual carbonyl−nitrosyl complexes of Rh^{2+} in Rh−ZSM-5: a combined FTIR spectroscopy and computational study. J Phys Chem C 111(28):10412–10418. https://doi.org/10.1021/jp067531f
19. Kunkeler PJ, Zuurdeeg BJ, Van Der Waal JC, van Bokhoven JA, Koningsberger DC, Van Bekkum H (1998) Zeolite beta: the relationship between calcination procedure, aluminum configuration, and Lewis acidity. J Catal 180(2):234–244. https://doi.org/10.1006/jcat.1998.2273
20. Drenchev NL, Chakarova KK, Lagunov OV, Mihaylov MY, Ivanova EZ, Strauss I, Hadjiivanov KI (2016) In situ FTIR spectroscopy as a tool for investigation of gas/solid interaction: water-enhanced CO_2 adsorption in UiO-66 metal-organic framework. MyJoVE Corporation, London. https://doi.org/10.3791/60285
21. Liu L, Zhao C, Miller JT, Li Y (2017) Mechanistic study of CO_2 photoreduction with H_2O on Cu/TiO_2 nanocomposites by in situ X-ray absorption and infrared spectroscopies. J Phys Chem C 121(1):490–499. https://doi.org/10.1021/acs.jpcc.6b10835
22. El-Roz M, Lakiss L, El Fallah J, Lebedev OI, Thibault-Starzyk F, Valtchev V (2013) Incorporation of clusters of titanium oxide in Beta zeolite structure by a new cold TiCl4-plasma process: physicochemical properties and photocatalytic activity. Phys Chem Chem Phys 15(38):16198–16207. https://doi.org/10.1039/C3CP52478G
23. Deo G, Turek AM, Wachs IE, Huybrechts DR, Jacobs PA (1993) Characterization of titania silicalites. Zeolites 13(5):365–373. https://doi.org/10.1016/0144-2449(93)90151-r
24. Fu C, Li F, Zhang J, Li D, Qian K, Liu Y, Huang W (2021) Site sensitivity of interfacial charge transfer and photocatalytic efficiency in photocatalysis: methanol oxidation on anatase TiO_2 nanocrystals. Angew Chem Int Ed 133(11):6225–6234. https://doi.org/10.1002/ange.202014037
25. Zhang H, Li Y, Wang J, Wu N, Sheng H, Chen C, Zhao J (2021) An unprecedent hydride transfer pathway for selective photocatalytic reduction of CO_2 to formic acid on TiO_2. Appl Catal B Environ 284:119692. https://doi.org/10.1016/j.apcatb.2020.119692
26. Subbotina IRF, Barsukov DVE (2020) Direct evidence of the key role of UV-formed peroxide species in photocatalytic gas–solid oxidation in air on anatase TiO_2 particles. Phys Chem Chem Phys 22(4):2200–2211. https://doi.org/10.1039/C9CP04728J
27. Hirakawa H, Hashimoto M, Shiraishi Y, Hirai T (2017) Selective nitrate-to-ammonia transformation on surface defects of titanium dioxide photocatalysts. ACS Catal 7:3713–3720. https://doi.org/10.1021/acscatal.7b00611
28. Dolamic I, Bürgi T (2007) Photocatalysis of dicarboxylic acids over TiO_2: an in-situ ATR-IR study. J Catal 248(2):268–276. https://doi.org/10.1016/j.jcat.2007.03.020
29. Almeida AR, Moulijn JA, Mul G (2011) Photocatalytic oxidation of cyclohexane over TiO_2: evidence for a Mars−Van Krevelen mechanism. J Phys Chem C 115(4):1330–1338. https://doi.org/10.1021/jp107290r
30. Almeida AR, Moulijn JA, Mul G (2008) In situ ATR-FTIR study on the selective photo-oxidation of cyclohexane over anatase TiO_2. J Phys Chem C 112(5):1552–1561. https://doi.org/10.1021/jp077143t
31. Belhadj H, Hakki A, Robertson PKJ, Bahnemann DW (2015) In situ ATR-FTIR study of H_2O and D_2O adsorption on TiO_2 under UV irradiation. Phys Chem Chem Phys 17:22940–22946. https://doi.org/10.1039/C5CP03947A
32. Telegeiev I, Thili O, Lanel A, Bazin P, Levaque Y, Fernandez C, El-Roz M (2018) In situ FTIR reactor for monitoring gas-phase products during a (photo) catalytic reaction in the liquid phase. Anal Chem 90(24):14586–14592. https://doi.org/10.1021/acs.analchem.8b04754

33. Li SY, Meng S, Zou X, El-Roz M, Telegeev I, Thili O, Zhu G (2019) Rhenium-functionalized covalent organic framework photocatalyst for efficient CO_2 reduction under visible light. Micropor Mesopor Mat 285:195–201. https://doi.org/10.1016/j.micromeso.2019.05.026
34. Nasrallah H, Lyu P, Maurin G, El-Roz M (2021) Highly efficient CO_2 reduction under visible-light on non-covalent Ru··· Re assembled photocatalyst: evidence on the electron transfer mechanism. J Catal 404:46–55. https://doi.org/10.1016/j.jcat.2021.09.007
35. Hess C (2021) New advances in using Raman spectroscopy for the characterization of catalysts and catalytic reactions. Chem Soc Rev 50(5):3519–3564. https://doi.org/10.1039/D0CS01059F
36. Ricci PC, Carbonaro CM, Stagi L, Salis M, Casu A, Enzo S, Delogu F (2013) Anatase-to-rutile phase transition in TiO_2 nanoparticles irradiated by visible light. J Phys Chem C 117(15):7850–7857. https://doi.org/10.1021/jp312325h
37. Swaminathan S, Rao VG, Bera JK, Chandra M (2021) The pivotal role of hot carriers in plasmonic catalysis of C−N bond forming reaction of amines. Angew Chem Int Ed 60(22):12532–12538. https://doi.org/10.1002/anie.202101639
38. Feng K, Wang Y, Guo M, Zhang J, Li Z, Deng T, Zhang Z, Yan B (2021) In-situ/operando techniques to identify active sites for thermochemical conversion of CO_2 over heterogeneous catalysts. J Energy Chem 62:153–171. https://doi.org/10.1016/j.jechem.2021.03.054
39. Chakrabarti A, Ford ME, Gregory D, Hu R, Keturakis CJ, Lwin S, Wachs IE (2017) A decade + of operando spectroscopy studies. Catal Today 283:27–53. https://doi.org/10.1016/j.cattod.2016.12.012
40. Kookhaee H, Tesema TE, Habteyes TG (2020) Switching a plasmon-driven reaction mechanism from charge transfer to adsorbate electronic excitation using surface ligands. J Phys Chem C 124(41):22711–22720. https://doi.org/10.1021/acs.jpcc.0c07479
41. Cheng Y, Wang W, Yao L, Wang J, Han H, Zhu T, Liang Y, Fu J, Wang Y (2020) 3D Ag/ZnO microsphere SERS substrate with ultra-sensitive, recyclable and self-cleaning performances: application for rapid in site monitoring catalytic dye degradation and insight into the mechanism. Colloids Surf A Physicochem Eng Asp 607:125507. https://doi.org/10.1016/j.colsurfa.2020.125507
42. Jiang P, Dong Y, Yang L, Zhao Y, Xie W (2019) Hot electron-induced carbon-halogen bond cleavage monitored by in situ surface-enhanced raman spectroscopy. J Phys Chem C 123(27):16741–16746. https://doi.org/10.1021/acs.jpcc.9b03238
43. Kumari G, Kamarudheen R, Zoethout E, Baldi A (2021) Photocatalytic surface restructuring in individual silver nanoparticles. ACS Catal 11(6):3478–3486. https://doi.org/10.1021/acscatal.1c00478
44. Qiu L, Pang GA, Zheng G, Bauer D, Wieland K, Haisch C (2020) Kinetic and mechanistic investigation of the photocatalyzed surface reduction of 4-nitrothiophenol observed on a silver plasmonic film via surface-enhanced raman scattering. ACS Appl Mater Interfaces 12(18):21133–21142. https://doi.org/10.1021/acsami.0c05977
45. Huang J, Niu W, Li C, Tan C, Yin P, Cheng H, Hu Z, Yang N, He Q, Nam G-H, Zhang H (2020) In-situ probing of crystal-phase-dependent photocatalytic activities of au nanostructures by surface-enhanced Raman spectroscopy. ACS Mater Lett 2(4):409–414. https://doi.org/10.1021/acsmaterialslett.0c00060
46. Zhang G, Chen L, Fu X, Wang H (2018) Cellulose microfiber-supported TiO_2@Ag nanocomposites: a dual-functional platform for photocatalysis and in situ reaction monitoring. Ind Eng Chem Res 57(12):4277–4286. https://doi.org/10.1021/acs.iecr.8b00006
47. Zhang H, Wei J, Zhang X-G, Zhang Y-J, Radjenovica PM, Wu D-Y, Pan F, Tian Z-Q, Li J-F (2020) Plasmon-induced interfacial hot-electron transfer directly probed by Raman spectroscopy. Chem 6(3):689–702. https://doi.org/10.1016/j.chempr.2019.12.015
48. Cai Z-F, Merino JP, Fang W, Kumar N, Richardson JO, De Feyter S, Zenobi R (2021) Molecular-level insights on reactive arrangement in on-surface photocatalytic coupling reactions using tip-enhanced Raman spectroscopy. JACS. https://doi.org/10.1021/jacs.1c11263
49. Rößler M, Huth PU, Liauw MA (2020) Process analytical technology (PAT) as a versatile tool for real-time monitoring and kinetic evaluation of photocatalytic reactions. React Chem Eng 5(10):1992–2002. https://doi.org/10.1039/D0RE00256A
50. Qian R, Zong H, Schneider J, Zhou G, Zhao T, Li Y, Pan JH (2019) Charge carrier trapping, recombination and transfer during TiO_2 photocatalysis: an overview. Catal Today 335:78–90. https://doi.org/10.1016/j.cattod.2018.10.053

51. Chiesa M, Giamello E, Livraghi S, Paganini MC, Polliotto V, Salvadori E (2019) Electron magnetic resonance in heterogeneous photocatalysis research. J Phys Condens Matter 31:444001. https://doi.org/10.1088/1361-648X/ab32c6
52. Zhang Y, Dai Y, Li H, Yin L, Hoffmann MR (2020) Proton-assisted electron transfer and hydrogenatom diffusion in a model system for photocatalytic hydrogen production. Commun Mater 1:66. https://doi.org/10.1038/s43246-020-00068-0
53. Park H, Ou H-H, Colussi AJ, Hoffmann MR (2015) Artificial photosynthesis of C1–C3 hydrocarbons from water and CO_2 on titanate nanotubes decorated with nanoparticle elemental copper and CdS quantum dots. J Phys Chem A 119:4658–4666. https://doi.org/10.1021/jp511329d
54. Bonke SA, Risse T, Schnegg A, Brückner A (2021) In situ electron paramagnetic resonance spectroscopy for catalysis. Nat Rev Methods Primers 1:33. https://doi.org/10.1038/s43586-021-00031-4
55. Al-Madanat O, Nunes BN, AlSalka Y, Hakki A, Curti M, Patrocinio AOT, Bahnemann DW (2021) Application of EPR spectroscopy in TiO_2 and Nb_2O_5 photocatalysis. Catalysts 11(12):1514. https://doi.org/10.3390/catal11121514
56. Zhang Y, Zhao J, Wang H, Xiao B, Zhang W, Zhao X, Liu Q (2022) Single-atom Cu anchored catalysts for photocatalytic renewable H2 production with a quantum efficiency of 56%. Nat Commun 13:58. https://doi.org/10.1038/s41467-021-27698-3
57. Shiraishi Y, Hashimoto M, Chishiro K, Moriyama K, Tanaka S, Hirai T (2020) Photocatalytic dinitrogen fixation with water on bismuth oxychloride in chloride solutions for solar-to-chemical energy conversion. J Am Chem Soc 142:7574–7583. https://doi.org/10.1021/jacs.0c01683
58. Koningsberger DC (1988) Principles, applications, techniques of EXAFS, SEXAFS and XANES. X-ray Absorp 20:20
59. Van Bokhoven JA, Lamberti C (2016) X-ray absorption and X-ray emission spectroscopy: theory and applications, vol 1. Wiley, New York
60. Singh J, van Bokhoven JA (2010) Structure of alumina supported platinum catalysts of different particle size during CO oxidation using in situ IR and HERFD XAS. Catal Today 155(3–4):199–205. https://doi.org/10.1016/j.cattod.2009.12.006
61. Deng J, Zhang Q, Lv X, Zhang D, Xu H, Ma D, Zhong J (2020) Understanding photoelectrochemical water oxidation with X-ray absorption spectroscopy. ACS Energy Lett 5(3):975–993. https://doi.org/10.1021/acsenergylett.9b02757
62. Coronado JM, Fresno F, Iglesias-Juez A (2021) Approaching photocatalysts characterization under real conditions: in situ and operando studies. Materials science in photocatalysis. Elsevier, New York, pp 139–156. https://doi.org/10.1016/B978-0-12-821859-4.00030-1
63. Zhao C, Liu L, Rao G, Zhao H, Wang L, Xu J, Li Y (2015) Synthesis of novel MgAl layered double oxide grafted TiO_2 cuboids and their photocatalytic activity on CO_2 reduction with water vapor. Catal Sci Technol 5(6):3288–3295. https://doi.org/10.1039/C5CY00216H
64. Hernández-Alonso MD, García-Rodríguez S, Suárez S, Portela R, Sánchez B, Coronado JM (2013) Operando DRIFTS study of the role of hydroxyls groups in trichloroethylene photo-oxidation over titanate and TiO_2 nanostructures. Catal Today 206:32–39. https://doi.org/10.1016/j.cattod.2012.01.029
65. Saqlain S, Cha BJ, Kim SY, Sung JY, Choi MC, Seo HO, Kim YD (2021) Impact of humidity on the removal of volatile organic compounds over Fe loaded TiO_2 under visible light irradiation: insight into photocatalysis mechanism by operando DRIFTS. Mater Today Commun 26:102119. https://doi.org/10.1016/j.mtcomm.2021.102119
66. Hernández-Alonso MD, Tejedor-Tejedor I, Coronado JM, Anderson MA (2011) Operando FTIR study of the photocatalytic oxidation of methylcyclohexane and toluene in air over TiO_2–ZrO_2 thin films: influence of the aromaticity of the target molecule on deactivation. Appl Catal B Environ 101(3–4):283–293. https://doi.org/10.1016/j.apcatb.2010.09.029
67. Bravo-Suárez JJ, Srinivasan PD (2017) Design characteristics of in situ and operando ultraviolet-visible and vibrational spectroscopic reaction cells for heterogeneous catalysis. Catal Rev 59(4):295–445. https://doi.org/10.1080/01614940.2017.1360071
68. Hernández-Alonso MD, Tejedor-Tejedor I, Coronado JM, Anderson MA, Soria J (2009) Operando FTIR study of the photocatalytic oxidation of acetone in air over TiO_2–ZrO_2 thin films. Catal Today 143(3–4):364–373. https://doi.org/10.1016/j.cattod.2009.02.033
69. El-Roz M, Kus M, Cool P, Thibault-Starzyk F (2012) New operando IR technique to study the photocatalytic activity and selectivity of TiO_2 nanotubes in air purification: influence of temperature, UV intensity, and VOC concentration. J Phys Chem C 116(24):13252–13263. https://doi.org/10.1021/jp3034819

70. Haselmann GM, Baumgartner B, Wang J, Wieland K, Gupta T, Herzig C, Eder D (2020) In situ Pt photodeposition and methanol photooxidation on Pt/TiO_2: Pt-loading-dependent photocatalytic reaction pathways studied by liquid-phase infrared spectroscopy. ACS Catal 10(5):2964–2977. https://doi.org/10.1021/acscatal.9b05588
71. Caudillo-Flores U, Muñoz-Batista MJ, Kubacka A, Fernández-García M (2018) Operando spectroscopy in photocatalysis. ChemPhotoChem 2(9):777–785. https://doi.org/10.1002/cptc.201800117
72. Muñoz-Batista MJ, Motta Meira D, Colón G, Kubacka A, Fernández-García M (2018) Phase-contact engineering in mono-and bimetallic Cu-Ni Co-catalysts for hydrogen photocatalytic materials. Angew Chem Int Ed 57(5):1199–1203. https://doi.org/10.1002/anie.201709552
73. Piccolo L, Afanasiev P, Morfin F, Len T, Dessal C, Rousset JL, Llorca J (2020) Operando X-ray absorption spectroscopy investigation of photocatalytic hydrogen evolution over ultradispersed Pt/TiO_2 catalysts. ACS Catal 10(21):12696–12705. https://doi.org/10.1021/acscatal.0c03464
74. Spanu D, Minguzzi A, Recchia S, Shahvardanfard F, Tomanec O, Zboril R, Altomare M (2020) An Operando X-ray absorption spectroscopy study of a $NiCu-TiO_2$ photocatalyst for H2 evolution. ACS Catal 10(15):8293–8302. https://doi.org/10.1021/acscatal.0c01373
75. Wu JC, Cheng YT (2006) In situ FTIR study of photocatalytic NO reaction on photocatalysts under UV irradiation. J Catal 237(2):393–404. https://doi.org/10.1016/j.jcat.2005.11.023
76. Wang K, Cao M, Lu J, Lu Y, Lau CH, Zheng Y, Fan X (2021) Operando DRIFTS-MS investigation on plasmon-thermal coupling mechanism of CO_2 hydrogenation on Au/TiO_2: the enhanced generation of oxygen vacancies. Appl Catal B Environ 296:120341. https://doi.org/10.1016/j.apcatb.2021.120341
77. Yan T, Wang L, Liang Y, Makaremi M, Wood TE, Dai Y, Ozin GA (2019) Polymorph selection towards photocatalytic gaseous CO_2 hydrogenation. Nat Commun 10(1):1–10. https://doi.org/10.1038/s41467-019-10524-2
78. Kataoka S, Tejedor-Tejedor MI, Coronado JM, Anderson MA (2004) Thin-film transmission IR spectroscopy as an in-situ probe of the gas–solid interface in photocatalytic processes. J Photochem Photobiol 163(3):323–329. https://doi.org/10.1016/j.jphotochem.2004.01.004
79. Lesage T, Verrier C, Bazin P, Saussey J, Daturi M (2003) Studying the NOx-trap mechanism over a Pt-Rh/Ba/Al2O3 catalyst by operando FT-IR spectroscopy. Phys Chem Chem Phys 5(20):4435–4440. https://doi.org/10.1039/B305874N
80. El-Roz M, Bazin P, Thibault-Starzyk F (2013) An operando-IR study of photocatalytic reaction of methanol on new* BEA supported TiO_2 catalyst. Catal Today 205:111–119. https://doi.org/10.1016/j.cattod.2012.08.023
81. Hamoud HI, Lafjah M, Douma F, Lebedev OI, Djafri F, Valchev V, El-Roz M (2019) Photo-assisted SCR over highly dispersed silver sub-nanoparticles in zeolite under visible light: an Operando FTIR study. Sol Energy 189:244–253. https://doi.org/10.1016/j.solener.2019.07.020
82. El-Roz M, Bazin P, Daturi M, Thibault-Starzyk F (2015) On the mechanism of methanol photooxidation to methylformate and carbon dioxide on TiO_2: an operando-FTIR study. Phys Chem Chem Phys 17(17):11277–11283. https://doi.org/10.1039/C5CP00726G
83. El-Roz M, Lakiss L, Telegeiev I, Lebedev OI, Bazin P, Vicente A, Valtchev V (2017) High-visible-light photoactivity of plasma-promoted vanadium clusters on nanozeolites for partial photooxidation of methanol. ACS Appl Mater Interfaces 9(21):17846–17855. https://doi.org/10.1021/acsami.7b02161
84. Wolski L, El-Roz M, Daturi M, Nowaczyk G, Ziolek M (2019) Insight into methanol photooxidation over mono-(Au, Cu) and bimetallic (AuCu) catalysts supported on niobium pentoxide—an operando-IR study. Appl Catal B Environ 258:117978. https://doi.org/10.1016/j.apcatb.2019.117978
85. Chen T, Ding Q, Wang X, Feng Z, Li C (2021) Mechanistic studies on photocatalytic overall water splitting over Ga2O3-based photocatalysts by operando MS-FTIR spectroscopy. J Phys Chem Lett 12(26):6029–6033. https://doi.org/10.1021/acs.jpclett.1c01621
86. Waheed A, Shi Q, Maeda N, Meier DM, Qin Z, Li G, Baiker A (2020) Strong activity enhancement of the photocatalytic degradation of an azo dye on Au/TiO_2 doped with FeOx. Catalysts 10(8):933. https://doi.org/10.3390/catal10080933
87. Chan HY, Nguyen VH, Wu J, Calvino-Casilda V, Bañares MA, Bai H (2015) Real-time Raman monitoring during photocatalytic epoxidation of cyclohexene over V-Ti/MCM-41 catalysts. Catalysts 5(2):518–533. https://doi.org/10.3390/catal5020518

88. Yan X, Xu Y, Tian B, Lei J, Zhang J, Wang L (2018) Operando SERS self-monitoring photocatalytic oxidation of aminophenol on TiO_2 semiconductor. Appl Catal B Environ 224:305–309. https://doi.org/10.1016/j.apcatb.2017.10.009
89. Guo S, Li Y, Tang S, Zhang Y, Li X, Sobrido AJ, Wei B (2020) Monitoring hydrogen evolution reaction intermediates of transition metal dichalcogenides via operando Raman spectroscopy. Adv Funct Mater 30(35):2003035. https://doi.org/10.1002/adfm.202003035
90. Wang QY, Chen YY, Ye RK, Liu Q, Chen HY, Yang H, Fang PP (2021) Instantly detecting catalysts' hot spots temperature in situ during photocatalysis by operando raman spectroscopy. Anal Chem 93(46):15517–15524. https://doi.org/10.1021/acs.analchem.1c03666
91. Agostini G, Meira D, Monte M, Vitoux H, Iglesias-Juez A, Fernandez-Garcia M, Gorges B (2018) XAS/DRIFTS/MS spectroscopy for time-resolved operando investigations at high temperature. J Synchrotron Radiat 25(6):1745–1752. https://doi.org/10.1107/S160057751801305X
92. Tsyganok A, Ghigna P, Minguzzi A, Naldoni A, Murzin V, Caliebe W, Ellis DS (2020) Operando X-ray absorption spectroscopy (XAS) observation of photoinduced oxidation in FeNi (oxy) hydroxide overlayers on hematite (α-Fe2O3) photoanodes for solar water splitting. Langmuir 36(39):11564–11572. https://doi.org/10.1021/acs.langmuir.0c02065
93. Fracchia M, Cristino V, Vertova A, Rondinini S, Caramori S, Ghigna P, Minguzzi A (2019) Operando X-ray absorption spectroscopy of WO3 photoanodes. Electrochim Acta 320:134561. https://doi.org/10.1016/j.electacta.2019.134561
94. Gao Y, Nie W, Wang X, Fan F, Li C (2020) Advanced space-and time-resolved techniques for photocatalyst studies. Chem Commun 56(7):1007–1021. https://doi.org/10.1039/C9CC07128H
95. Paz Y (2019) Transient IR spectroscopy as a tool for studying photocatalytic materials. J Phys Condens Matter 31(50):503004. https://doi.org/10.1088/1361-648X/ab3eda
96. Li Q, Anpo M, Wang X (2020) Application of photoluminescence spectroscopy to elucidate photocatalytic reactions at the molecular level. Res Chem Intermed 46(10):4325–4344. https://doi.org/10.1007/s11164-020-04209-5
97. Miao TJ, Tang J (2020) Characterization of charge carrier behavior in photocatalysis using transient absorption spectroscopy. J Chem Phys 152(19):194201. https://doi.org/10.1063/5.0008537
98. Van Schrojenstein Lantman EM, Deckert-Gaudig T, Mank AJ, Deckert V, Weckhuysen BM (2012) Catalytic processes monitored at the nanoscale with tip-enhanced Raman spectroscopy. Nat Nanotechnol 7(9):583–586. https://doi.org/10.1038/nnano.2012.131
99. Dürr RN, Maltoni P, Tian H, Jousselme B, Hammarstrom L, Edvinsson T (2021) From NiMoO4 to γ-NiOOH: detecting the active catalyst phase by time resolved in situ and operando Raman spectroscopy. ACS Nano 15(8):13504–13515. https://doi.org/10.1021/acsnano.1c04126
100. Piercy VL, Saeed KH, Prentice AW, Neri G, Li C, Gardner AM, Cowan AJ (2021) Time-resolved Raman spectroscopy of polaron formation in a polymer photocatalyst. J Phys Chem Lett 12(44):10899–10905. https://doi.org/10.1021/acs.jpclett.1c03073
101. Ismail AS, Uemura Y, Park SH, Kwon S, Kim M, Elnaggar H, De Groot FM (2020) Direct observation of the electronic states of photoexcited hematite with ultrafast 2p3d X-ray absorption spectroscopy and resonant inelastic X-ray scattering. Phys Chem Chem Phys 22(5):2685–2692. https://doi.org/10.1039/C9CP03374B
102. Baran T, Fracchia M, Vertova A, Achilli E, Naldoni A, Malara F, D'Acapito F (2016) Operando and time-resolved X-ray absorption spectroscopy for the study of photoelectrode architectures. Electrochim Acta 207:16–21. https://doi.org/10.1016/j.electacta.2016.04.153
103. Lai TH, Katsumata KI, Hsu YJ (2021) In situ charge carrier dynamics of semiconductor nanostructures for advanced photoelectrochemical and photocatalytic applications. Nanophotonics 10(2):777–795. https://doi.org/10.1515/nanoph-2020-0472
104. Zhang M, De Respinis M, Frei H (2014) Time-resolved observations of water oxidation intermediates on a cobalt oxide nanoparticle catalyst. Nat Chem 6(4):362–367. https://doi.org/10.1038/nchem.1874
105. Sheng H, Oh MH, Osowiecki WT, Kim W, Alivisatos AP, Frei H (2018) Carbon dioxide dimer radical anion as surface intermediate of photoinduced CO_2 reduction at aqueous Cu and CdSe nanoparticle catalysts by rapid-scan FT-IR spectroscopy. JACS 140(12):4363–4371. https://doi.org/10.1021/jacs.8b00271
106. Sheng H, Frei H (2016) Direct observation by rapid-scan FT-IR spectroscopy of two-electron-reduced intermediate of tetraaza catalyst [CoIIN4H (MeCN)]2+ converting CO_2 to CO. JACS 138(31):9959–9967. https://doi.org/10.1021/jacs.6b05248

107. Andersen LK, Frei H (2006) Dynamics of CO in mesoporous silica monitored by time-resolved step-scan and rapid-scan FT-IR spectroscopy. J Phys Chem B 110(45):22601–22607. https://doi.org/10.1021/jp0640326
108. Colbeau-Justin C, Valenzuela MA (2013) Time-resolved microwave conductivity (TRMC) a useful characterization tool for charge carrier transfer in photocatalysis: a short review. Rev Mex Fís 59(3):191–200
109. Toe CY, Lamers M, Dittrich T, Tahini HA, Smith SC, Scott J, Ng YH (2022) Facet-dependent carrier dynamics of cuprous oxide regulating the photocatalytic hydrogen generation. Mater Adv 3(4):2200–2212. https://doi.org/10.1039/D1MA00934F
110. Wei Z, Wang W, Li W, Bai X, Zhao J, Tse EC, Zhu Y (2021) Steering electron-hole migration pathways using oxygen vacancies in tungsten oxides to enhance their photocatalytic oxygen evolution performance. Angew Chem Int Ed 60(15):8236–8242. https://doi.org/10.1002/anie.202016170
111. Portela R, Perez-Ferreras S, Serrano-Lotina A, Bañares MA (2018) Engineering operando methodology: understanding catalysis in time and space. Front Chem Sci Eng 12(3):509–536. https://doi.org/10.1007/s11705-018-1740-9

Publisher's Note Springer Nature remains neutral with regard to jurisdictional claims in published maps and institutional affiliations.

Authors and Affiliations

Houeida Issa Hamoud[1] · Lukasz Wolski[2] · Ilia Pankin[3] · Miguel A. Bañares[4] · Marco Daturi[1] · Mohamad El-Roz[1]

[1] Laboratoire Catalyse et Spectrochimie, Normandie Université, ENSICAEN, UNICAEN, CNRS, 14050 Caen, France

[2] Faculty of Chemistry, Adam Mickiewicz University, Uniwersytetu Poznańskiego 8, 61-614 Poznań, Poland

[3] Smart Materials, Research Institute, Southern Federal University, Sladkova Street 174/28, 344090 Rostov-on-Don, Russia

[4] Catalytic Spectroscopy Laboratory, Instituto de Catalisis, ICP-CSIC, 28049 Madrid, Spain